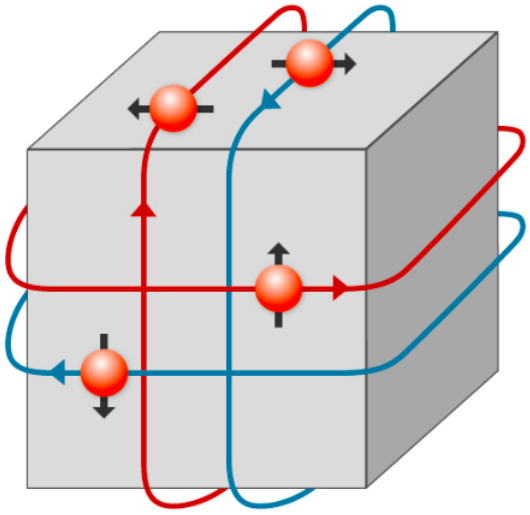

1

Bismuth Thin Film Growth on Salts and the Pursuit of Topological Insulators

THESIS

submitted in partial fulfillment of the
requirements for the degree of

BACHELOR OF SCIENCE
in
PHYSICS

Author :	Dyon van Dinter
Student ID :	1514229
Supervisor :	Prof. dr. J. M. van Ruitenbeek
2^{nd} corrector :	Prof. dr. J. Aarts

Leiden, The Netherlands, July 17, 2017

Bismuth Thin Film Growth on Salts and the Pursuit of Topological Insulators

Dyon van Dinter

Huygens-Kamerlingh Onnes Laboratory, Leiden University
P.O. Box 9500, 2300 RA Leiden, The Netherlands

July 17, 2017

Abstract

The search for topological insulators has intensified over the last couple of years. One of the candidates theorized to be a topological insulator are bilayers of bismuthene, the bismuth analogue of graphene. During the bachelor project, multiple thin films of Bismuth were grown and their quality under the influence of underlying substrates of $NaCl(001)$ and $BaF_2(111)$ has been investigated. Growth was achieved in a high vacuum Thermal Evaporator. The topography of substrates and grown films were analyzed using Atomic Force Microscopy. A large part of the project was focused on restoring a UHV system in which thin films could be grown and analyzed. This system will help improve the quality of the films and therefore improves the chances of producing a sufficiently large sample for electronic measurements. The cleaved barium-fluoride produces ultra-flat plateaus optimal for growth. The grains grown on the barium-fluoride substrates were larger in two-dimensional sizes than the grains grown on sodium-chloride. Further research is required to obtain the crystalline configuration of these grains.

[1]Coverpicture by Paul Scherrer Institute/Mahir Dzambegovic [1].

Contents

Chapter 1

Introduction: Bismuth Thin Films and Topological Insulators

The interest in topological insulators has grown exponentially in the last couple of decades, mainly because of its promising applications. To name just a few; the topological insulator might be a promising candidate in the race to produce a stable Majorana Fermion which can be used for making a Quantum Computer. They might also play a role in future energy transportation because of the dissipation-less conductance of electrons in edge states. On top of this, this characteristic could be usefull in the field of nano-electroncs. Another intriguing feature is the spin-filtered nature of the edge states, a promising characteristic that may be used in the field of *spintronics* [2].

However, one of the big obstacles yet to overcome is the ability to grow a large enough sample to be used for the production of devices. In the particular case, Bismuth, we desire a large enough sample which has the same single crystalline structure and which is atomically flat. A lot of research on Bismuth has already been done, such as the growth of Bismuth on $Si(111)$-7×7 [3], $NaCl(001)$ [4] and $BaF_2(111)$ [5]. In this project, the growth of Bismuth thin films on substrates of $NaCl(001)$ and $BaF_2(111)$ has been investigated.

To introduce the world of topological insulators, an introduction of an analogy which describes the characteristics of this exotic state of matter quite accurately might be useful. Imagine a crowded inner city with lots of traffic in which nobody is getting anywhere in their cars. The entire inner city is stuck in a huge traffic jam, but luckily for a few happy souls, the city has an effective ring-road. This ring-road is so effective, that one does not even burn fuel when driving on this road. No traffic accidents will ever occur on this road. When standing between the two lanes, one would always see a stream of white-front headlights coming his way at the left and a stream of red-back headlights going the opposite direction at the right. This analogy captures the essence of a topological insulator (TI). One could view the entire city as being a 2D TI. The cars are the electrons and as known for a TI, it is non-conductive in the bulk (the crowded inner city). But at the edge (the ring-road), something interesting happens; the electrons are allowed to move in an ordered fashion without energy dissipation. The streams are spin-filtered, which means the direction of the stream is correlated to the spin of the electrons. This is what was described by the observation of the headlights in the analogy. But as with all analogies, the city analogy has it's flaws and doesn't encapsulate all the aspects and subtleties of the TI. The theoretical framework will dive more into depth concerning the several requirements and facets of this state of matter.

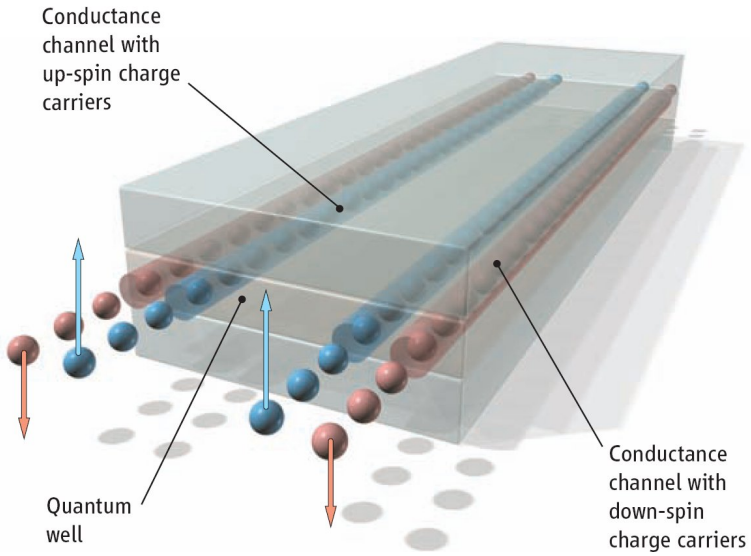

Figure 1.1: *Example of a Quantum Spin Hall Insulator as theorized by Bernevig [6] and experimentally verified by Molenkamp [7] in HgTe Quantum Wells. Adapted from Ref [7].*

Chapter 2

Description of the Research Question and Hypothesis

2.1 Description of the Research Question

The research question in a growth study can be formulated in various ways. In this bachelor project, multiple research questions were tackled. The critical and most relevant ones are formulated down below:

- Which substrate benefits the growth of the desired crystalline structure, $Bi(111)$?
- How does the flatness of the substrate influence the growth of the Bismuth thin films?
- What is a possible physical explanation for the possibly encountered favoritism?

The main research question of this bachelor project is: *"Which underlying substrate influences the growth of the Bismuth thin films in such a way that the production of sufficiently large samples with the correct crystalline configuration, $Bi(111)$, becomes achievable."*

Grown films that are crystalline $Bi(111)$ and have dimensions of at least 100×100 nano-meter are considered to be sufficient. This is because ultimately, the strived end-goal is to measure the electronic properties of the topological insulator. This can be achieved through the fabrication of a *Quantum Hall bar* out of the grown sample. But this fabrication is only possible once the sample has suffiently large dimensions. Furthermore, the choice for the substrates $NaCl(001)$ and $BaF_2(111)$ hasn't been made arbitrarly. The underlying substrates influence the electrical measurements if they conduct electricity themselves. Thus the choice for insulators such as these salts is justified. On top of this, promising results on these substrates have already been accomplished [4, 5].

2.2 Hypothesis

The hypothesis is based on the fact that the growth of Bismuth thin films on $NaCl$ and BaF_2 has already been done. The Bismuth thin film are expected to grow in different orientations because of rotational symmetry of the lattice and the lattice potential of the substrate. However, which substrate is favored by the Bismuth thin film, depents largely on the underlying lattice. To truly make an educated guess, one should run computer simulations that factor in the lattices and their potentials. It is expected that the lattice potential plays a crucial role in this favouritism.

With an atomically flat surface, one would expect the thin film grown in a thermal evaporator to be flat as well (up to a certain degree). However, the desired crystalline configuration is theorized to be subjugated to the rotational and translational symmetry of the underlying substrate lattices.

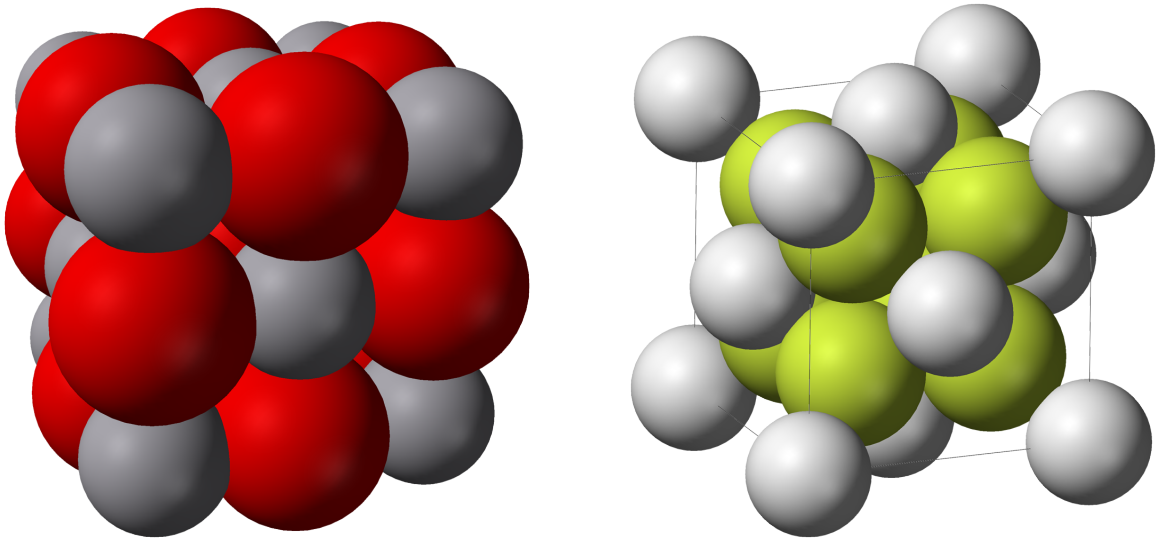

Figure 2.1: *The lattice structure of $NaCl$ is represented on the left [8]. The red spheres represent chlorine atoms and the gray spheres represent sodium atoms. Secondly, the lattice structure of BaF_2 is shown on the right [9]. The yellow spheres represent fluorine atoms and the gray spheres represent barium atoms.*

Because both lattices show rotational symmetry of 90 degrees in the (001)-plane, the crystalline configuration is predicted to form different grains rotated accordingly.

Chapter 3

Theoretical framework

The theory of topological insulators finds its basis in the mathematical field of *Topology* [10]. This is the description of matchematical objects and spaces undergoing smooth deformations and its applications have shown to be powerful tools for physicists. In condensed matter physics, it has often occurred that an exotic state of matter was first experimentally encountered. This resulted in fueling theoretical physicists to come up with a theoretical framework. In the case of topological insulators, the conventional chronological order was converted. The existence of this state was first predicted theoretically before it was verified experimentally.

Moreover, the basic phenomenology of a TI is simple: in two dimensions one could speak of a surface which is exclusively conductive at the edges. Such a two dimensional state of matter is called the Quantum Spin *Hall* Insulator State. The 3D analogy of the TI is straightforward, they do not conduct electricity in the bulk, but they are conductive on the surface. The transportation of electrons at the surface (edge) is spin-filtered because of Spin-Orbit Coupling (SOC) and topologically protected by time-reversal symmetry (TRS). This means that back-scattering is not a possibility for the electrons and this will result in dissipation-less transport [11].

However, to obtain a better understanding in the Topology of Topological insulators, the Integer Quantum *Hall* Effect (IQHE) will be formulated. This effect is basically the TRS breaking version of the TI. After this paragraph, a thorough description of the topology and symmetry that play a key-role in topological insulators and the Quantum Spin *Hall* Effect (QSHE) shall follow. A model shall be introduced, the topological invariant of the TI will be mentioned and the importance of spin-orbit coupling shall be verified. Lastly, a short section shall be dedicated to the structure and band spectrum of $Bi(111)$ and thin film growth.

3.1 The Integer Quantum *Hall* Effect

In this section, the mathematical formulation of the Integer Quantum *Hall* Effect shall be discussed, since it has a lot of similarities with the QSHE. This formulation gives an educative insight in the field of topological phases and should help the reader to get a better understanding in the connection between *Condensed Matter* and *Topology*.

First of all, the formulation of the *Berry* Phase and how it plays an important role in the description of topological phases such as the IQHE will be given. The *Berry* Phase will support the introduction of topological invariants, invariants that have a central part in this story. In this section, the topological invariant of the IQHE through using Berry's formulation will be encountered. The mathematical formulation in this chapter was largely summarized from the Colloquium by C. L. Kane and M. Z. Hassan [12] and the review paper by Y. Ando [13].

3.1.1 The *Berry* Phase

We define **R**(t) to be a set of time-dependent parameters and we shall consider it as a vector in the parameter space. The Schrödinger equation for this system is given by:

$$H[\mathbf{R}(t)]|n,\mathbf{R}(t)\rangle = E_n[\mathbf{R}(t)]|n,\mathbf{R}(t)\rangle \tag{3.1}$$

The Hamiltonian is specified by the parameter **R**(t) as H[**R**(t)] and the nth eigenstate is given by $|n,\mathbf{R}(t)\rangle$. The time evolution is as usual given given by the time-dependent Schrödinger equation. When we change **R** adiabatically from the $t = 0$ value $\mathbf{R}_0$ we get a time evolution that follows:

$$H[\mathbf{R}(t)]|n,t\rangle = i\hbar\frac{\partial}{\partial t}|n,t\rangle \tag{3.2}$$

And the state at a different time t is given by:

$$|n,t\rangle = \exp(\frac{i}{\hbar}\int_0^t L_n[\mathbf{R}(t')]\ \mathrm{d}t')|n,\mathbf{R}(t)\rangle \tag{3.3}$$

In which we defined the $L_n[\mathbf{R}(t)]$ as:

$$L_n[\mathbf{R}(t)] = i\hbar\dot{\mathbf{R}}(t)\cdot\langle n,\mathbf{R}(t)|\nabla_R|n,\mathbf{R}(t)\rangle - E_n[\mathbf{R}(t)] \tag{3.4}$$

The dot is known as the time derivative and the ∇_R operator is the gradient.

One may now write the time-dependent state by plugging equation 3.4 into 3.3 and we arrive at the following equation:

$$|n,t\rangle = \exp(-\int_0^t i\hbar\dot{\mathbf{R}}(t')\cdot\langle n,\mathbf{R}(t')|\nabla_R|n,\mathbf{R}(t')\rangle\ \mathrm{d}t')|n,\mathbf{R}(t)\rangle \tag{3.5}$$

$$\times\exp(\frac{i}{\hbar}\int_0^t E_n[\mathbf{R}(t')\ \mathrm{d}t')$$

Now, when we let $\mathbf{R}$ move on a closed loop C from $t=0$ and return to its initial starting point to close the loop at $t=T$, the *Berry* Phase is defined by the quantum-mechanical phase accumulation during the time evolution as is given by:

$$\gamma_n[C] = \int_0^T \dot{\mathbf{R}}(t)\cdot i\langle n,\mathbf{R}(t)|\nabla_R|n,\mathbf{R}(t)\rangle\ \mathrm{d}t \tag{3.6}$$

$$= \oint_C i\langle n,\mathbf{R}|\nabla_R|n,\mathbf{R}\rangle\cdot\ \mathrm{d}\mathbf{R} \tag{3.7}$$

$$= -\oint_C \mathbf{A}_n(\mathbf{R})\cdot\ \mathrm{d}\mathbf{R} \tag{3.8}$$

$$= -\int_S \mathbf{B}_n(\mathbf{R})\cdot\ \mathrm{d}\mathbf{S} \tag{3.9}$$

The connection between the last two lines is established through Stokes' theorem. The *Berry* connection is here defined as:

$$\mathbf{A}_n(\mathbf{R}) = -i\langle n,\mathbf{R}|\nabla_R|n,\mathbf{R}\rangle \tag{3.10}$$

and the *Berry* curvature is defined as the rotation of the *Berry* connection:

$$\mathbf{B}_n(\mathbf{R}) = \nabla_R\times\mathbf{A}_n(\mathbf{R}) \tag{3.11}$$

The description of the *Berry* Phase will help us to understand the topological invariants that occur in the IQHE and the QSHE and, in the end, how these invariants give rise to those states of matter.

3.1.2 The $TKNN$ invariant

The $TKNN$ (Thouless, Kohomoto, Nightingale and den Nijs) invariant is the topological invariant defined for the IQHE and is closely related to the *Berry* Phase. In the following paragraph, this close relation will be made apparent by deriving the $TKNN$ invariant. In this derivation, the *Hall* conductivity will be calculated of a 2D electron system of size $L \times L$ and subjugated to a perpendicular magnetic and electric field. The electric field E shall be applied along the y-axes, the magnetic field B shall be applied along the z-axes. Furthermore, one could treat the effect of the electric field as a perturbation potential $V = -eEy$ and this gives rise to approximating the perturbed eigenstate as:

$$|n\rangle_E = |n\rangle + \sum_{m \neq n} \frac{\langle m|(-eEy)|n\rangle}{E_n - E_m}|m\rangle + ... \tag{3.12}$$

Now the expectation value of the current density along the x-axes, can simply be obtained by:

$$\langle j_x\rangle_E = \sum_n f(E_n)\langle n|_E(\frac{ev_x}{L^2})|n\rangle_E = \langle j_x\rangle_{E=0} + \frac{1}{L^2}\sum_n f(E_n) \tag{3.13}$$
$$\times \sum_{m \neq n}\left(\frac{\langle n|(ev_x)|m\rangle\langle m|(-eEy)|n\rangle}{E_n - E_m} + \frac{\langle n|(-eEy)|m\rangle\langle m|(ev_x)|n\rangle}{E_n - E_m}\right)$$

In this formula, v_x is defined as the electron velocity along the x-axis and $f(E_n)$ is known as the Fermi distribution function.

By using the Heisenberg equation of motion:

$$\frac{d}{dt}y = v_y = \frac{1}{i\hbar}(E_n - E_m)[y, H] \tag{3.14}$$

this shall lead to:

$$\langle m|v_y|n\rangle = \frac{1}{i\hbar}(E_n - E_m)\langle m|y|n\rangle \tag{3.15}$$

Now we can evaluate the *Hall* conductivity:

$$\sigma_{xy} = \frac{\langle j_x \rangle_E}{E} = -\frac{i\hbar e^2}{L^2} \sum_{n \neq m} f(E_n) \times \frac{\langle n|v_x|m\rangle\langle m|v_y|n\rangle - \langle n|v_y|m\rangle\langle m|v_x|n\rangle}{(E_n - E_m)^2} \tag{3.16}$$

And by using Bloch's theorem [14] in which we consider a system in a periodic potential with the Bloch states described by $|u_{n\mathbf{k}}\rangle$ and using the following identity:

$$\langle u_{m\mathbf{k'}}|v_\mu|u_{n\mathbf{k}}\rangle = \frac{1}{\hbar}(E_{n\mathbf{k}} - E_{m\mathbf{k'}})\langle u_{m\mathbf{k'}}|\frac{\partial}{\partial k_\mu}|u_{n\mathbf{k}}\rangle \tag{3.17}$$

We arrive at the following equation for the *Hall* conductivity:

$$\sigma_{xy} = -\frac{ie^2}{\hbar L^2} \sum_{\mathbf{k}} \sum_{m \neq n} f(E_{n\mathbf{k}}) \times (\frac{\partial}{\partial k_x}\langle u_{n\mathbf{k}}|\frac{\partial}{\partial k_y}|u_{n\mathbf{k}}\rangle - \frac{\partial}{\partial k_y}\langle u_{n\mathbf{k}}|\frac{\partial}{\partial k_x}|u_{n\mathbf{k}}\rangle) \tag{3.18}$$

In terms of Bloch states, the *Berry* connection described in the previous paragraph is written as:

$$\mathbf{a}_n(\mathbf{k}) = -i\langle u_{n\mathbf{k}}|\nabla_k|u_{n\mathbf{k}}\rangle = -i\langle u_{n\mathbf{k}}|\frac{\partial}{\partial \mathbf{k}}|u_{n\mathbf{k}}\rangle \tag{3.19}$$

One should be able to recognize the *Berry* connection in formula 3.17 and this allows us to reduce the *Hall* conductivity to a compact form:

$$\sigma_{xy} = \nu\frac{e^2}{h} \tag{3.20}$$

In which ν is defined as:

$$\nu = \sum_n \int_{BZ} \frac{\mathrm{d}^2\mathbf{k}}{2\pi}(\frac{\partial a_{n,y}}{\partial k_x} - \frac{\partial a_{n,x}}{\partial k_y}) \tag{3.21}$$

Moreover, one could express ν as the summation of the contribution from the individual nth band, thus $\nu = \sum_n \nu_n$. This shall make the relation with the *Berry* phase more apparent:

$$\nu_n = \int_{BZ} \frac{\mathrm{d}^2\mathbf{k}}{2\pi}\left(\frac{\partial a_{n,y}}{\partial k_x} - \frac{\partial a_{n,x}}{\partial k_y}\right) \tag{3.22}$$

$$= \frac{1}{2\pi}\oint_{\partial BZ} \mathbf{a}_n(\mathbf{k}) \cdot \mathrm{d}\mathbf{k} = -\frac{1}{2\pi}\gamma_n[\partial BZ]$$

In this case, the wave function is single-valued, because after encircling the Brillouin zone it returns to its initial value. This results in the fact that the change in phase factor after encircling the Brillouin zone boundary, which we called ∂BZ, can only be an integer multiple of 2π:

$$\gamma_n[\partial BZ] = 2\pi m \qquad (m \in \mathbb{Z}) \tag{3.23}$$

Thus, ν_n can only take an integer value and therefore ν can only take an integer value. This leads to the effect that the *Hall* conductivity σ_{xy} is quantized to integer multiples of e^2/h. The integer value ν is what we call the *TKNN* invariant. This invariant is identical to the *Chern number* [15], which is defined as the total *Berry* flux in the Brillouin zone. In the next section, the necessary ingredients that make up a topological insulator and how they give rise to the QSHE shall be named and explained. This shall be an intensive elaboration on the topology and symmetries of these systems.

3.2 The Quantum Spin *Hall* Effect

As mentioned previously, the Integer Quantum *Hall* system could be interpreted as a TI with time-reversal symmetry breaking due to the presence of an external magnetic field. This reasoning can also be done the other way around, one could view the TI as an Quantum *Hall* system that does respect time-reversal symmetry due to the absence of an external magnetic field. But one may now ask what makes the QSHE a *topological* state of matter. To answer this question, an elaborate description of the topology in condensed matter systems will be made. To do this properly, a zero dimensional system known as a *Quantum Dot* will be introduced and the effect of the important uphold symmetry, known as *time-reversal symmetry*, shall be described.

Lastly, the topological invariant of TIs, the Z_2 invariant [16], and an educative explanation of the importance of spin-orbit coupling are given.

3.2.1 Topology in Condensed Matter Physics

To give an appropriate view of the topology and symmetry in our topological band theory, imagine a zero-dimensional system known as a quantum dot [17]. This quantum system has a finite number of states N and its Hamiltonian is represented by a hermitian $N \times N$ - matrix H. The real eigenvalues E_n are the eigenvalues of the Hamiltonian operator working on state $|n\rangle$. The quantum dot can be viewed as in the following image.

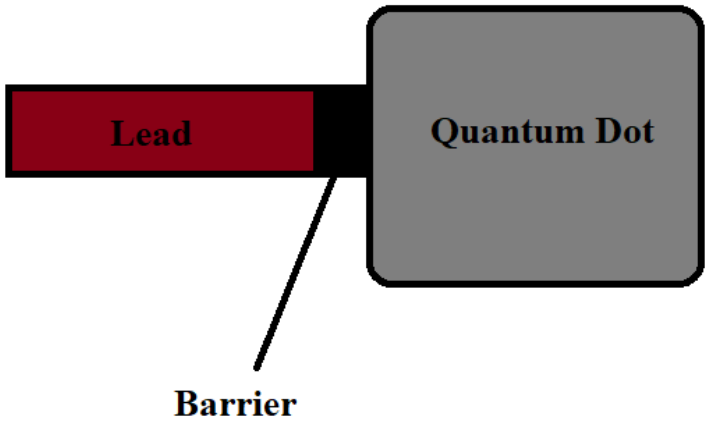

Figure 3.1: *Our zero-dimensional system, the Quantum Dot.*

A metallic lead is connected to the quantum dot in order for us to be able to measure the energies E_n with respect to the Fermi level E_F. For the sake of simplicity, we will set $E_F = 0$. This will lead to the fact that all positive energies E_n are represented by empty states, and negative energies E_n by filled states. The lead and dot are separated by a potential barrier, in order for them to be coupled weakly so we can see the system as being isolated to a certain degree [17] .

As mentioned by C.L. Kane: *"One of the objects of topological band theory is to classify topologically distinct Hamiltonians $H(\boldsymbol{k})$"* [11]. What is meant with this specific sentence shall be made clear shortly. Topology is the field of mathematics concerned with the properties of space while undergoing smooth deformations [10]. In the context of condensed matter physics, one could ask oneself if the Hamiltonians of two distinct quantum systems can be continuously deformed into each other. If this is the case, then the two systems are what is called *topologically equivalent*.

However, all Hamiltonians would be topologically equivalent if we consider them without constraints. If we restrict ourselves to Hamiltonians with an energy gap, this changes in a drastic fashion and now it should be possible to topologically distinguish Hamiltonians. The constraint we are going to apply is as follows: we say that two gapped quantum systems are topologically equivalent if their Hamiltonians can be continuously deformed into each other without ever closing the energy gap. An example in topology is the topological equivalence of the surface of a dough-nut and the surface of a coffee mug. One could continuously deform one into the other and thus they are topologically equivalent with respect to some topological invariant. However, the surface of a sphere and the surface of a doughnut cannot be smoothly deformed into each other without making an extra hole. Therefore, they are topologically inequivalent and they are distinguished by a topological invariant called the *genus* g. The formation of extra holes is analog to the closing of the energy gap in our band theory.

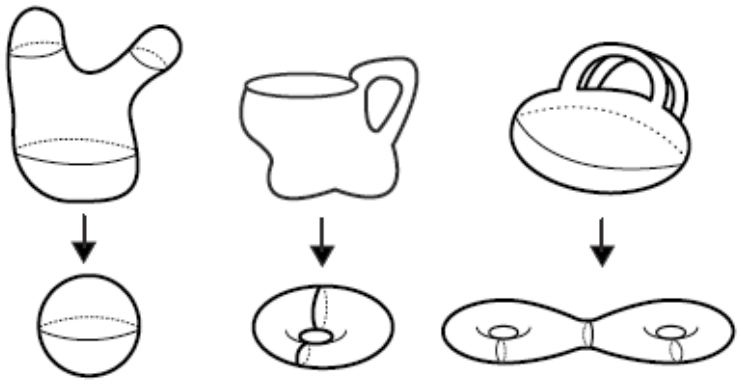

Figure 3.2: *Examples of topological smooth deformations. From left to right, the genus of the portrait surfaces is equal to the amount of holes in the bottom surfaces, thus $g = 0, 1$ and 2 from left to right respectively [18].*

Thus we should be able to define a topological invariant for our quantum system that describes the possibility of smoothly deforming one Hamiltonian into another one without closing the energy gap. If they have the same topological invariant,

this should be possible. If one counts the number of filled energy states ($E_n < 0$), one should be able to imagine that continuous transformations between Hamiltonians only exist if they have the same number of energy levels below zero. This is how we define our topological invariant at the moment: *"The number of energy levels below zero; an unchangeable invariant under continuous deformation inside the set op gapped Hamiltonians. We shall call this invariant Q"*.

Now, a *topological phase transition* is simply defined as a change in Q. One could count the number of zero-energy crossings in the spectrum of a Hamiltonian and whenever a zero-crossing occurs, the number of levels below zero changes and as a result, Q changes. Keep in mind that two types of zero-crossings occur: one with a positive group velocity (from $E < 0$ to $E > 0$) and one with a negative group velocity (from $E > 0$ to $E < 0$). If the number of "negative" zero-crossings is equal to the "positive" zero-crossings, Q will remain unchanged. However, if the two Hamiltonians have a different topological invariant, they must be separated by a transition. It is impossible to go from one to the other without closing the energy gap. Let's look at a brief example to portray the idea of the topological invariant Q.

Imagine that our quantum dot is simply described by a real-valued and random 10×10-matrix Hamiltonian. Let's now deform H into another Hamiltonian H' by varying an external parameter α and by parameterizing the deformation in the following way.

$$H(\alpha) = \alpha H' + (1 - \alpha)H \tag{3.24}$$

In which we let α run from 0 to 1. This parameterization obeys the initial condition, $(H(0) = H)$ and the final condition $(H(1) = H')$. By looking at the spectrum of the Hamiltonian, we can analyze the behavior of the energy levels while undergoing deformation.

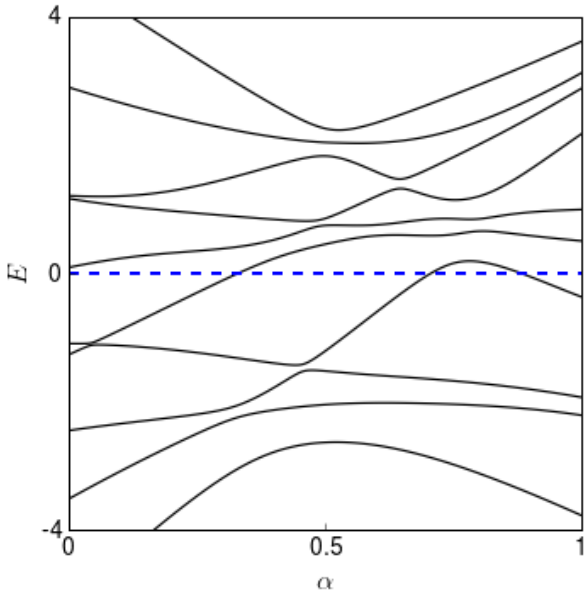

Figure 3.3: *Spectrum of the Hamiltonian while applying deformation. The deformation is parametrized by equation 3.24. The spectrum clearly shows two positive zero-crossings and one negative zero-crossing, resulting in a change of Q. Adapted from Ref [17].*

Looking at the spectrum, we can clearly see a change in Q while deforming the Hamiltonian. When we plot the value of Q as a function of parameter α, we should be able to conclude that the topological invariant of the initial Hamiltonian and the resulting Hamiltonian differ.

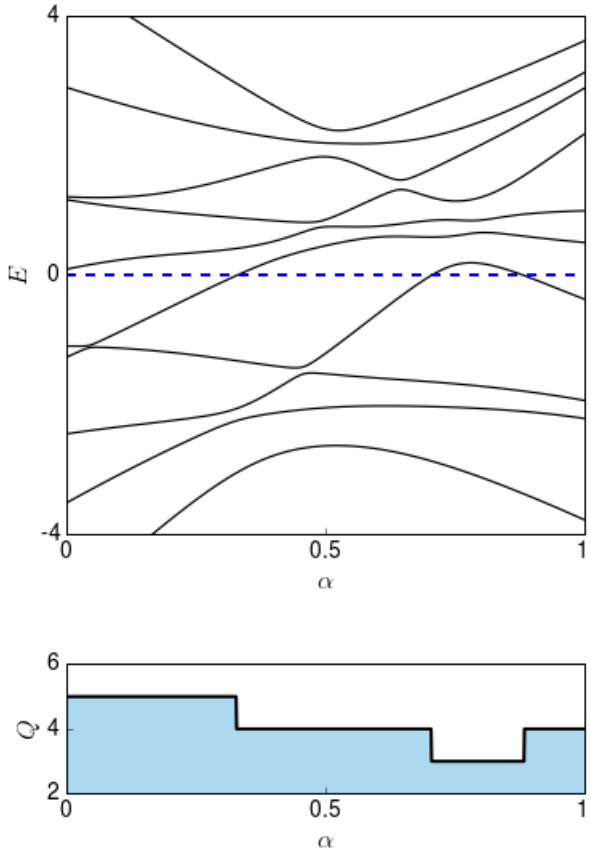

Figure 3.4: *Spectrum of the Hamiltonian as a function of parameter α and the resulting change in topological invariant Q as a function of α. Adapted from Ref [17].*

Thus the two Hamiltonians H and H' are not topologically equivalent. They have to be separated by a topological phase transition and therefore the energy gap must close somewhere. This of course is a specific and simplified example developed to portray the topological invariant Q. This invariant could be used to classify Hamiltonians in a topological manner, exactly what Kane [11] spoke of.

3.2.2 Topology and Time-Reversal Symmetry

Admittedly, the previous Hamiltonian wasn't taken to be real-valued by accident. Real-valued Hamiltonians are manifestations of time-reversal symmetry. This is known as the symmetry of physical laws under the transformation of time reversal. But now the Hamiltonian should also take complex valued entries into account. For systems with $\frac{1}{2}$-spin particles, the TRS operator has the form $\Theta = i\sigma_y K$ in which σ_y is a Pauli matrix and K is the complex conjugate operator. One could easily check that $\Theta^2 = -1$. A Hamiltonian that obeys this type of time-reversal symmetry must also obey:

$$H = \sigma_y H^* \sigma_y \tag{3.25}$$

This gives rise to an interesting effect. Hamiltonians with this kind of TRS are *Kramer degenerate* [11]: every energy eigenvalue E_n is now doubly degenerate. The consequences for the topological invariant Q are implicit, the topological invariant Q can now only take even values due to TRS. Thus time-reversal symmetry has a direct effect on the topology of the system, but it is far from the only symmetry that could influence the topological invariant [17].

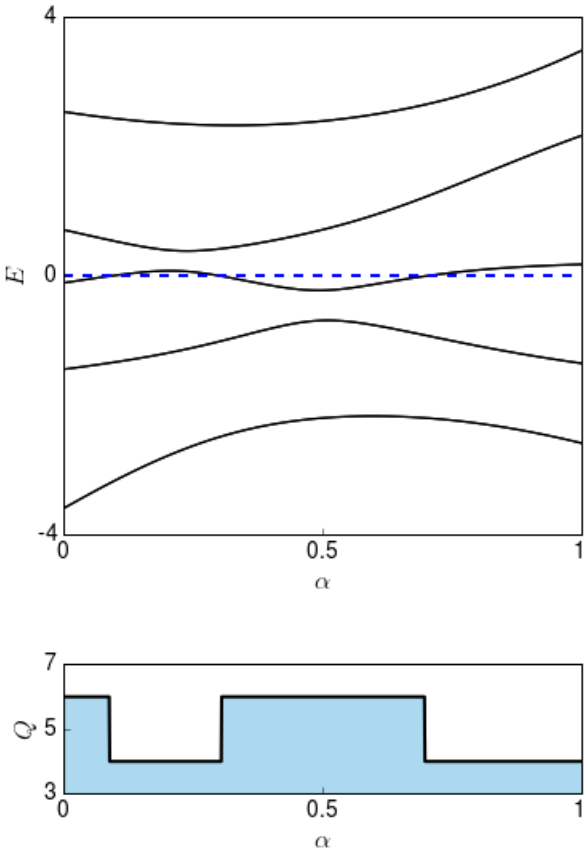

Figure 3.5: *Spectrum of a Hamiltonian obeying time-reversal symmetry and Kramers' Theorem. The spectrum and topological invariant Q are plotted as a function of parameter α. Adapted from Ref [17].*

3.2.3 The Z_2 Invariant of Topological Insulators

For topological insulators, there are multiple ways to mathematically describe their invariants. However, all of them share the same analogy with the invariant Q as seen in the previous paragraph. One way to mathematically formulate the invariant is to define a unitary matrix using the time-reversal operator Θ:

$$w_{mn}(\mathbf{k}) = \langle u_m(\mathbf{k})|\Theta|u_n(\text{-}\mathbf{k})\rangle \tag{3.26}$$

In this specific case, the value of our topological invariant switches between 0, the trivial phase and 1, the topological phase. These invariant changes are caused by the previously named zero-crossings. Now this invariant can be calculated by a mathematical object called the *Pfaffian* [19]. When a zero-crossing happens, the sign of the Pfaffian changes and this alters the invariant. The invariant change that occurs at a single zero-crossing point, denoted by Λ_a, can be calculated by:

$$\delta_a = \frac{Pf[w(\Lambda_a)]}{\sqrt{Det[w(\Lambda_a]}} = \pm 1 \tag{3.27}$$

There are four special points in the two dimensional case that can change the sign of the Pfaffian and that one needs to take into account. Therefore, our topological invariant Z_2, known as ν, is defined as:

$$(-1)^{\nu} = \prod_{a=1}^{4} \delta_a \tag{3.28}$$

This formulation can be extended to the three dimensional form through incorporating more points where zero-energy crossings can occur [11]. One of the strengths of this invariant is that it can be calculated form the bulk-Hamiltonian. If the topological invariant has a value of 1, one could expect edge modes to occur at the boundary of the medium. This is precisely what is meant with the *bulk-boundary correspondence*. Furthermore, the formula for the Z_2 invariant can also be expressed in terms of the *Berry* curvature [20]. This is a mathematical task that will not be conducted in this thesis.

3.2.4 The importance of Spin-Orbit Coupling

Thus far, we have not considered the spin-freedom. Through an effect called *spin-orbit coupling*, we shall give rise to the physical cause of zero-crossings and thus the change in topological invariant. Spin-orbit coupling is a relativistic effect, because it involves electrons with high velocities. Similarly in comparison to what happens in the case of the IQHE effect, when an electron with momentum $\mathbf{p}$ moves in a magnetic field $\mathbf{B}$, it shall experience a Lorentz force in the direction perpendicular to its motion given by the formula:

$$\mathbf{F} = -e\mathbf{p} \times \mathbf{B}/m \tag{3.29}$$

Now the electron possesses an energy equal to $\mu_B \sigma \cdot \mathbf{B}$, named the *Zeeman Energy*. In this formula, e and m are known as the electron charge and mass respectively, and μ_B is the Bohr magneton. The σ is defined as the vector of the Pauli spin matrices. When one takes a look at the electron, which moves in the electric field of the nucleus, it can be noticed from the reference frame transformation that it experiences a magnetic field in its reference frame of $\mathbf{B}_{eff} \sim \mathbf{E} \times \mathbf{p}/mc^2$. This field induces a momentum-dependent Zeeman Energy called the spin-orbit coupling and is equal to:

$$H_{SOC} = \frac{\hbar}{4m^2c^2}(\mathbf{p} \times \mathbf{E})\sigma \tag{3.30}$$

Furthermore, in the context of a 2D topological insulator, the strong SOC shall cause the uppermost valence sub-band to split. Now this sub-band is above the bottom sub-band in the conduction band and results in band inversion. In contrast with the IQHE, the QSHE does exists at zero magnetic field and is protected by time-reversal symmetry, which is a property preserved by SOC [21]. The spin-coupling also locks the momentum to the spin and must always point perpendicular to it. In this way two *spin-filtered* edge states arise.

Moreover, the importance of the preservation of time-reversal symmetry by SOC and how it prevents backscattering from happening is a crucial property. The conducting states are insensitive to non-magnetic disorder and impurities because there are no states available for back-scattering. Without any back-scattering, the transportation of the edge states shall be dissipation-less.

3.3 Thin Films of $Bi(111)$ and Topological Insulators

3.3.1 Crystalline and Band Structure of $Bi(111)$

As explained in the previous section, a material with strong spin-orbit coupling is required such that the Hamiltonian is topologically non-trivial in a certain region. It has been theorized and computed, that bilayers of $Bi(111)$ shall exhibit the Quantum Spin *Hall* Effect [13]. The structure of truncated $Bi(111)$ is presented below.

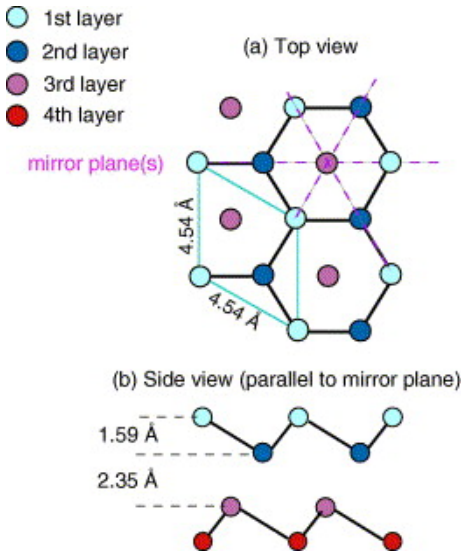

Figure 3.6: *The truncated-bulk structure of Bi(111). The bilayers are formed by covalent bonds indicated by black solid lines. Figure (a) shows us the top view of the first three layers. The lattice constants are given and the striped purple lines represent the mirror planes. It is evident from this view that each layer consists of a two-dimensional trigonal lattice. Figure (b) portrays the side view of four layers. The formation of bilayers is clearly shown in this representation. This figure is taken from a review paper by Ph. Hofmann: The surfaces of bismuth: Structural and electronic properties [22].*

The splitting due to strong spin-orbit coupling intensifies when one approaches the surfaces and gives rise to the splitting of the surface states as can be seen in the band structure in figure 3.7. This splitting leads to the zero-energy crossings of the bands. As discussed in the previous section, this is exactly what changes our topological invariant.

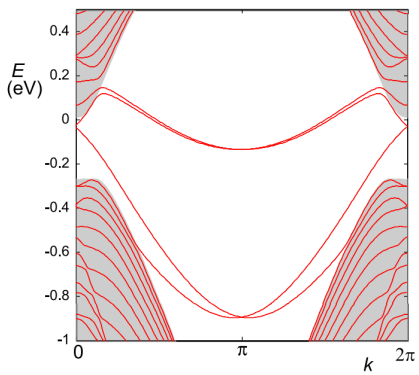

Figure 3.7: *Bandstructure of 2D $Bi(111)$ with the mentioned zero-crossings. This spectrum was obtained through calculations using the bilayer tight-binding model of bismuth in the (111)-plane. Adapted from Ref [23].*

3.3.2 The Growth of Thin Films

The way in which thin film grow is of importance to the goal of this project. Therefore, this paragraph is dedicated to a short description of what kinds of growth occur and how the underlying substrate influences these kinds of growth. Three main different growth modes are at play here: *Frank-van der Merwe* mode (layer by layer), *Stranski-Krastanov* mode (layer plus islands) and the *Volmer-Weber* mode (islands) [24].

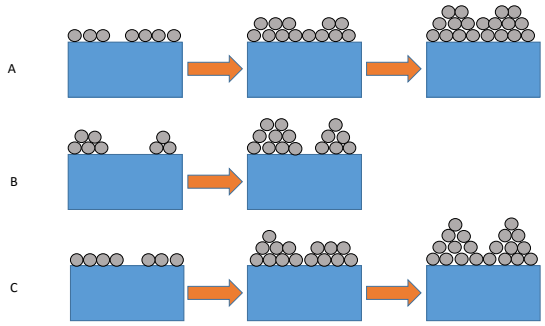

Figure 3.8: *A graphical representation of the three main growth modes: Frank-van der Merwe mode (A), the Volmer-Weber mode (B) and Stranski-Krastanov mode (C).*

The preferred mode of growth is influenced by the substrate in different ways because changing the specific kind of substrate changes several factors. To name just a few: the lattice potential changes, the lattice constants are likely to differ (and therefore the matching with the film is asymmetric), capillary forces are influenced and the new substrate is more or less vulnerable to wetting. Besides the influence of substrates, other factors also play a role in which growth mode is preferred, such as growth rate and substrate temperature. To truly give an educative guess on the preferred mode in the set-up and how to change this, one would need to run computer simulations.

In the following chapter, an elaboration on the experimental set-up and methods shall be made. Multiple techniques will be introduced and the operation procedures shall be explained.

Chapter 4

Experimental Set-Up and Methods

In this chapter, the experimental set-up and methods used in the bachelor project shall be thoroughly illustrated. A wide variety of techniques and machines have been used, but the focus shall mainly be on the *Atomic Force Microscope* (AFM) and the *Thermal Evaporator*.

For the sake of the logical flow of this thesis, this chapter shall commence with outlining the standard sample preparation. This will be followed by a description of the measurement and growth activities in a chronicle fashion.

However, a large part of the project was spent on working on an ultra-high vacuum (UHV) system in the measurement hall called the JEOL. The JEOL combines a variety of measurement techniques while also achieving growth through the usage of a Knudsen cell. The specifications and benefits of this set-up shall be described at the end of this chapter.

4.1 Sample Preparation

At the start of the project, the focus was largely on getting acquainted with the sample preparation and measurement techniques. During this training, the usage of silicon wafers was common. These were cut with a diamond knife to an appropriate size (5×5 mm). These silicon samples were organically cleaned in the clean room. The cleaning process was carried out as described below:

- Firstly, dirt on the sample surface was removed by rinsing the samples with acetone. After intensive rinsing, they were put in a glass beaker filled with acetone. This beaker was placed in an ultrasonic bath and was kept there to undergo vibrational cleaning for 5 minutes.
- Secondly, this process was repeated with iso-propanol. The samples were rinsed and directly placed in a beaker filled with iso-propanol. Again, this beaker was placed in the ultrasonic bath and left to undergo treatment for 5 minutes.
- Lastly, the samples were taken out of the ultrasonic bath and dried with compressed nitrogen. Their cleanliness was checked under an optical microscope in the clean room. If they were cleaned up to a satisfactory degree, these samples would be used as substrates for growth.

However, the sample preparation of other substrates besides silicon, such as $NaCl$ and BaF_2, was executed differently due to the differences in solubility in the used chemicals. A brief description of their individual preparation before they were used as substrates for growth shall now be summarized.

- $NaCl$ substrates were firstly measured in the AFM to check the surface flatness. We improved the surface flatness of these substrates by spin-coating them with distilled water in the spin-coater in the clean-room. To remove residual water, they were spin-coated again, but this time with iso-propanol. Afterwards, we verified the improvement in surface flatness by checking the morphology of the surface in the AFM.
- BaF_2 substrates were also initially checked concerning their surface flatness in the AFM. By cleaving the samples along the (111)-plane before doing growth, we ensured the atomically flat morphology of the substrates. As with the $NaCl$, the flatness was investigated with the AFM.

4.2 Atomic Force Microscopy

In nano- and surface sciences, Atomic Force Microscopy (AFM) is a commonly used technique to measure the topography and morphology of surfaces. It is a type of Scanning Probe Microscopy (SPM) which resolution surpasses the diffraction limit for optical systems. The resolution achieved by AFM can be in the order of nanometers or smaller and thus gives us an excellent way to determine the flatness of a surface to an enormous accuracy. In the context of this project, the surface flatness of the substrates is of crucial importance due to the effect it would have on the growth of the Bismuth thin films. Therefore, substrates with atomically flat surfaces were preferable. In this section, the basic principles of AFM and our specific measurement procedures with the JPK AFM shall be clarified.

4.2.1 Basic Principles of AFM

As mentioned earlier, AFM is a scanning probe technique. But in contrast with the well-known *Scanning Tunneling Microscope*, the AFM has the ability to do measurements on insulators. This can be achieved because instead of relying on *quantum tunneling* such as the STM does, the AFM is based on a set of phenomena apart from conduction. This makes the AFM technique very suitable for the measurements on our substrates and the insulating regime of TIs. As the name implies, it relies on the forces between atoms such as electrostatic forces, mechanical contact forces and *van der Waals* forces. Due to its volatility, the AFM can be used for different purposes, imaging being the most relevant one for this project. However, it can also be used to manipulate the surface of a sample as is done in atomic manipulation or scanning probe lithography. Another useful feature is the ability to perform force spectroscopy in which one could determine the cohesion forces between individual molecules. The focus shall exclusively be made on the imaging methods used by the AFM to obtain a topography map of sample surfaces.

A simplified and basic configuration for an atomic force microscope can be seen on the next page. An AFM generally consists of a laser, a photo-diode (usually with four quadrants), cantilever with microscopic tip and a piezoelectric scanner. The sample is placed on this scanner in order to move the surface around with steps in the order of nanometers. As the sample moves under the tip, the tip and cantilever are attracted or repelled due to the atomic forces between the probe and surface. The movement of the cantilever is then registered as a displacement of the laser spot on the photo-diode. This can be translated into topographic data of the surface. Most commonly used in AFM imaging is a feedback loop to keep the force between the probe and surface constant. The input of this feedback is the cantilever deflection and its output controls the distance between sample and probe. As the cantilever is scanning the surface, the separation between probe and surface is continuously adjusted to keep the cantilever deflection, called the set-point, constant. By doing this, the atomic force between sample and probe is kept constant. This set-point value of the cantilever deflection can be predefined by the user and determines how rough the cantilever is scanning the surface. In this case, the feedbacks output represents the topography of the surface up to a certain error. Moreover, there are a lot of varieties in modes in which

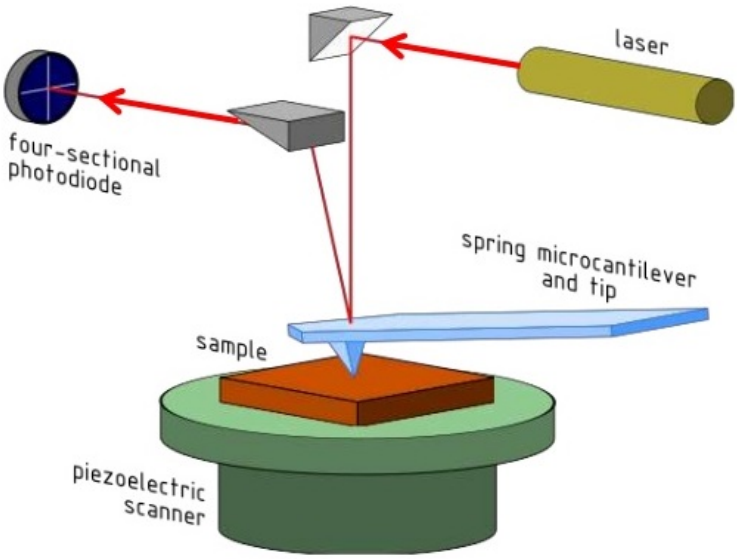

Figure 4.1: *A standard AFM configuration. The inner reflection of the laser by mirrors might differ in different microscopes, but the basic principles remain the same.*

the AFM can operate, all with their respective advantages and disadvantages. Our images were acquired by using AC mode. This is commonly referred to as the *tapping mode*. In the AC mode, the cantilever is oscillating up and down with a frequency chosen to be near its resonance frequency. The big advantage of this mode is that it enables us to detect short range forces in ambient conditions without our tip sticking to the liquid layer formed on the surface. This gives the reader a rough idea of the principles on which the AFM relies [25]. The measurement procedures undertaken to operate the atomic force microscope shall be targeted next. The AFM operated in this project is mainly the JPK AFM located at the LION SPM User Facility of Leiden University.

4.2.2 Measurement Procedures of the JPK AFM

Before doing the actual measurements, the samples were prepared as described in section 4.1. The next step is mounting the cantilever holder with a correct cantilever. These can differ in resonance frequency and depending on the type of measurements one wants to conduct, one should chose a cantilever with a suitable resonance frequency. Once the cantilever holder with cantilever is mounted on the AFM head, the laser alignment commences. With an optical microscope, one can verify the position of the laser spot and place it correctly on the tip of the cantilever. Here, an example of correct positioning of the laser can be seen.

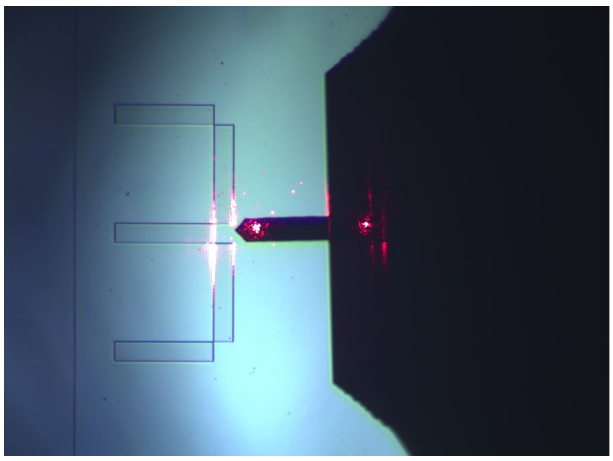

Figure 4.2: *Example of a successfully executed laser alignment [26].*

When the laser spot is positioned on the tip of the cantilever, the spot is reflected and must fall on the photo-diode. The lateral and vertical deflection must be minimized while maximizing the total signal. This can be achieved by moving the photo-diode or by changing the angle of the mirror which reflects the light from the cantilever onto the photo-diode. The next step is to carry out a frequency sweep to find the exact resonance frequency of the cantilever. This information is needed to chose the driving frequency in AC mode. Not one cantilever is exactly alike and thus the resonance frequency will differ from the value given by the manufacturer. One can now insert the driving frequency and set-point. The driving frequency of the cantilever is chosen to be slightly smaller than the actual resonance frequency and the set-point is chosen to be around 70-80 % of the corresponding driving amplitude. The set-point value can be changed during scanning in order to tap harder or more gently onto the surface, thus influencing image quality. But one also influences the risk of breaking the cantilever while changing the set-point.

If a suitable driving frequency and set-point is inserted, the approach can start. At first, the probe will be separated from the surface with a distance in the order of centimeters. One can control the Z motor of the AFM head manually to approach the sample with bigger steps. Though, one should keep in mind that the feedback is not running while doing this fast approach and therefore you should be extra careful not to crash the tip into the surface. When the cantilever has approached the sample close enough, the feedback approach can commence. This means the piëzo of the cantilever

is continuously extending and retracting while oscillating the tip at the driving frequency. If the amplitude of the cantilevers oscillation is unchanged after extending the piëzo all the way, the cantilever is clearly not in contact with the surface. Therefore the probe can approach the surface with a length equal to the piëzos range. Once the approach is successful, the oscillation amplitude will be affected by the atomic forces between probe and sample. If the oscillation amplitude has changed enough to surpass the predefined set-point, the approach is halted and completed. One should check if the actual approach was successful by retracting the tip and repeating the approach.

Before the actual imaging can start, the gain of the feedback should be adjusted appropriately. The gain has an direct effect on the scanning. For instance, if the gain is too low with respect to the scan speed, the cantilever will have difficulties following the contours of the surface. This will also cause the trace and retrace of your system to significantly differ. This can be solved by repeatedly scanning an individual line while altering the gain. Once the trace and retrace have converged to a satisfying degree, the actual imaging can begin.

4.3 Thin Film Growth and Thermal Evaporation

After the surfaces of the samples were characterized with the AFM, they were used as substrates for the growth of Bismuth thin films. This growth was accomplished by thermal evaporation. This is a commonly used thin-film deposition technique and it relies on the evaporation and condensation of source material in vacuum. The way in which evaporation can be attained differ from resistive to flash evaporation or by using an electron-beam to heat the source material. The thermal evaporator used in this project achieved evaporation by means of resistive heating. The basic principles of thermal resistive evaporation and the specific growth procedures shall be discussed in this section.

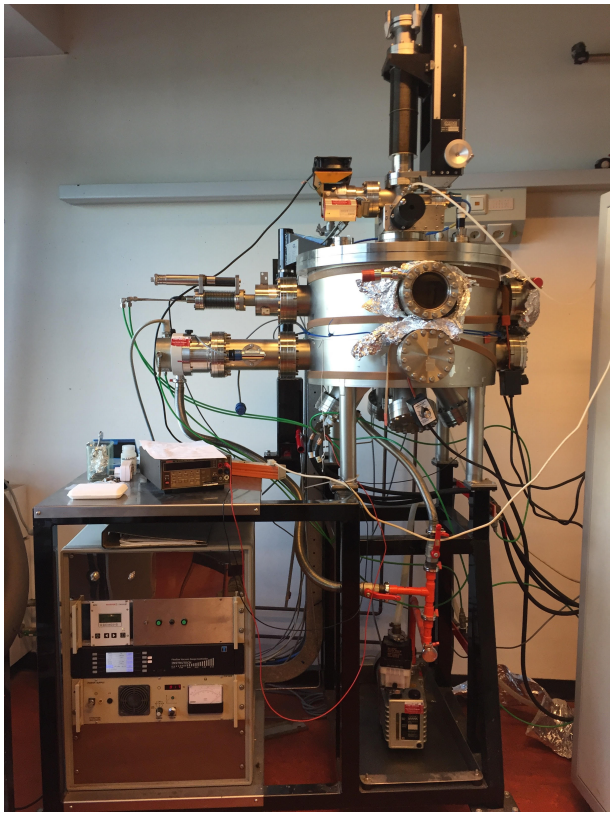

Figure 4.3: *The thermal evaporator that was used during the bachelor project. This machine is custom build and used by several research groups of LION.*

4.3.1 Basic Principles of Thermal Resistive Evaporation

As mentioned above, thermal evaporation is a growth technique of thin films. The source material is heated by resistive heating and as a result the material evaporates. Resistive heating is nothing more then letting a high current pass through the source material and in this way, due to its *resistance*, heating it to high temperatures. But only a fraction of the evaporated material condenses on the substrate and forms a thin film. These two main processes, evaporation and condensation, take place in high vacuum. This causes the evaporated material to move in a ballistic fashion with an enlarged

mean free path. Thus the probability of an evaporated particle colliding with another particle is decreased and this enhances the uniformity of ones thin film. A basic set-up of an thermal resistive evaporator (TRE) consists of the following components.

- The *load-lock*, separated from the evaporation chamber by a removable valve, in which the sample is loaded. This prevents the main vacuum from having to rise to atmospheric pressure when loading a sample.
- The *evaporation chamber* in which the actual evaporation and thus growth is accomplished.
- A *quartz sensor* used to monitor the thickness of the grown film and the growth rate is located in the evaporation chamber.
- Sufficient *roughing pumps* and *turbos* to attain the desired vacuum.
- *Pressure (ion) gauges* used to monitor the pressure in the load-lock and evaporation chamber.
- *Source material* that will desirably compose the actual grown film. In this case, the source material was Bismuth.
- A *shutter* to prevent growth on the substrate before a stable growth rate is accomplished.
- *Power supplies* which deliver a satisfactory current to achieve evaporation of the source material by resistive heating.

These components form the basis of a standard thermal resistive evaporator. A schematic overview of this system can be seen on the next page. However, the quality and uniformity of the grown film is limited by several factors.

- The quality of the vacuum restricts the quality of the grown film. The lower the vacuum, the lower the collision probability of particles and the higher the quality of the film.
- The purity of the source material also effects the quality of the end-product. When the source material itself is impure, one could expect the deposited film to be impure as well.
- Due to the geometry of the evaporator and the substrate, the thickness of the film will differ in different places.

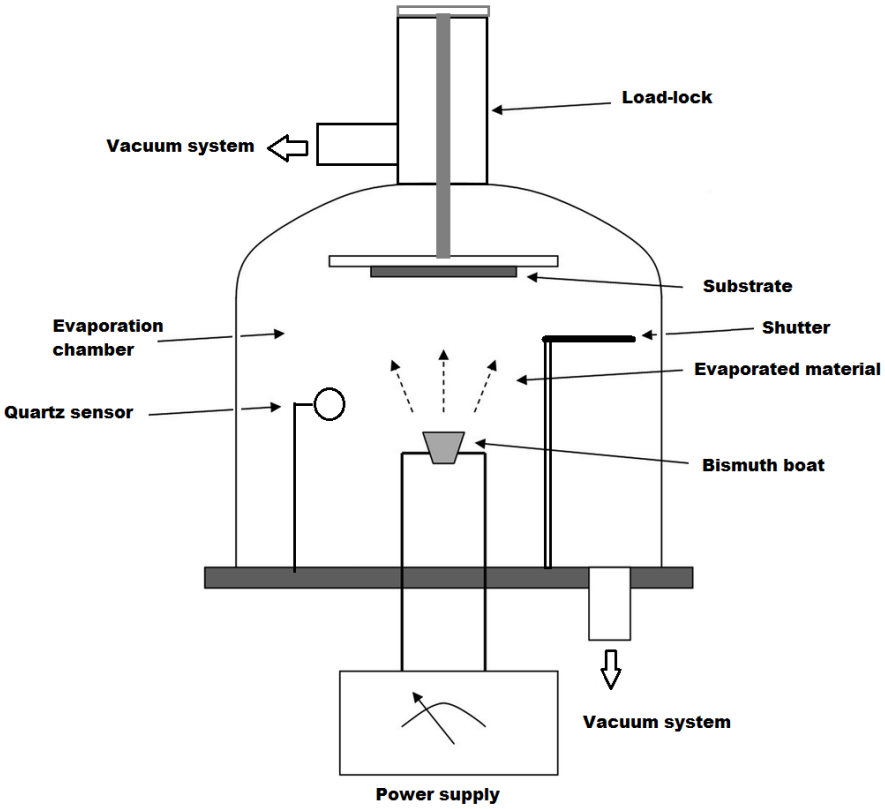

Figure 4.4: *A schematic overview of the configuration of a Thermal Resistive Evaporator [27].*

Therefore, we could improve the quality of our film by using very pure source material, attaining a high vacuum ($10^{-7} - 10^{-8}$ mbar) to increase the mean free path and by implementing a tooling factor. The tooling factor corrects for the difference of material deposited on the substrate versus the quartz sensor. This is due to the geometry of the evaporation chamber and substrate. Because the material is evaporated uniformly, the material spreads out like the inverse of $4\pi d^2$, in which d is the distance between source material and the condensation location [28]. From this it is easy to see that when the substrate is further away from the source material than the quartz sensor, the thickness of the grown film on the substrate will be less in comparison with what was grown on the crystal. The tooling factor for a specific system can be calculated using:

$$T_{factor} = T_{approx} \times \frac{d_{actual}}{d_{quartz}} \tag{4.1}$$

In which T_{factor} is the calculated tooling factor, T_{approx} is the approximate tooling factor (which can be set to 100% if unknown), d_{actual} is the actual thickness grown on the substrate measured by an independent system (such as an AFM) and d_{quartz} is the thickness of the grown film as indicated by the quartz crystal. For the specific system of this project, the tooling factor turned out to be 21%. In the following paragraph, the growth procedures undertaken to form a thin film of Bismuth on the substrates will be explained.

4.3.2 Growth Procedures of the TRE

After the substrate sample was organically cleaned in the clean-room and characterized by the JPK AFM, it would be ready for growth. The load-lock and evaporation chamber were separated by closing a valve. Furthermore, the line to the roughing pump would be closed. The turbo connected to the load-lock would be switched off and spinned down by letting a little nitrogen flow in. Once the turbo had stopped spinning, the nitrogen flow was increased to bring the load-lock to atmospheric pressure. The samples were tightened to the sample holder and the sample holder was placed back in the load-lock.

Figure 4.5: *The used sample holder of the TRE. The contours clearly show the placement of previous samples.*

The load-lock would then be firmly closed by ISO-clamps and pumped down to a vacuum of at least 10^{-6} mbar. This was achieved by firstly closing the line to the evaporation chamber turbo, so that the overpressure wouldn't damage it. Now the line to the roughing pump could be reopened. When a pressure of 10^{-1} mbar was reached, the load-lock turbo could be switched on. Once the vacuum was around the 10^{-3} mbar, the line to the evaporation chamber turbo could be reopened. This would increase the total pumping rate and when the pressure was below 10^{-6} mbar, the valve between the load-lock and evaporation chamber could be opened.

Now the sample holder could be turned down into place. The shutter would be kept in front of the sample before a stable and desired growth rate was attained. The Bismuth boat was selected and the correct density, tooling factor and z-factor would be inserted in the controller of the quartz sensor. The next step was turning on the power supplies and slowly heating the source material. The voltage over the source material was registered with a multimeter while heating it. Once heating was completed and the desired growth rate was achieved and stable, the shutter was removed and growth on the actual substrate would commence. With the quart sensor, the grown thickness

was monitored and after the preferred thickness was reached, the shutter would be placed in front of the sample again.

Lastly, the sample would be taken out of the system by turning the sample holder up and by bringing the separated load-lock back to atmospheric pressure. Once the grown samples were removed, the sample holder would be placed back into the load-lock and this would be pumped down to vacuum once more.

4.4 JEOL: Ultrahigh Vacuum Atomic Force Microscope

As mentioned at the beginning of this chapter, a large part of the project was spent restoring an ultra-high vacuum atomic force microscope. The official name of this UHV AFM is the JSPM-4500A, but in the Van Ruitenbeek research group it is also known as the JEOL. The AFM feature is by far not the only functionality of the JEOL. In this section, a short description will be given of all the different features of this specific JEOL.

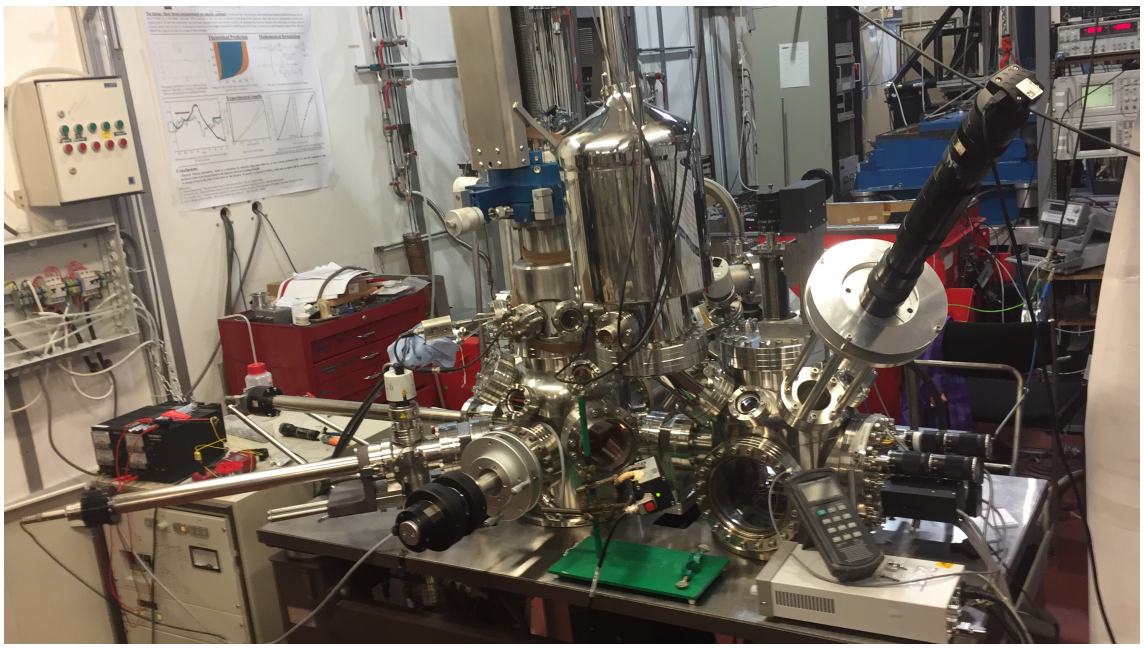

Figure 4.6: *The JEOL in the measurement hall of Leiden University. This specific machine differs form the standard JSPM-4500A model. An elaboration on these differences will be implemented in this section.*

4.4.1 Capabilities of the JEOL system

The standard JSPM-4500A model has the possibility of conducting AFM and STM measurements. However, the system has been adjusted to incorporate growth (Knudsen Cell) and electron diffraction (LEED). In this system, everything can be done *in situ*, from substrate analysis and growth, to analyzing the thin film itself.

Firstly, the ultra-high vacuum environment is illustrated. The system has been open for over a year and therefore one would expect the inside to be filled with water and other undesired contaminations. After closing the system, the roughing pump and turbo started with lowering the pressure. When the pressure was around the value of $10^{-6} - 10^{-7}$ mbar, the ion pumps could be started. Due to the out-gassing of water and other molecules in the chambers, it would take a long time to arrive at the desired pressure and the chambers would remain contaminated. To get rid of these particles and water layers, one would have to execute a *bake-out*, in which the

complete system is heated up to a temperature of around the 100 degrees Celsius. This will greatly increase the out-gassing rate of the particles inside the system and as an effect, the pressure would rise. Nevertheless, if one waits long enough, most of the contaminations would have been out-gassed and pumped away. Consequently, the pressure would gradually decrease once more. As the system cools down after the bake-out, the out-gassing rate will drop as well and this causes the pressure to further improve. With this procedure, pressures in the order of magnitude $10^{-8} - 10^{-9}$ mbar can be easily reached. To truly arrive in the range of ultra-high vacuum, the *titanium sublimation pumps* (TSP) must be operated frequently. The TSP sublimates titanium by periodically letting a high current pass through its filament. The titanium is very reactive and bonds the particles inside the chamber to the chamber wall. This will have a positive effect on the vacuum of the system. Through this entire process, the pressure of the main chamber and AFM chamber could be monitored using pressure gauges. It could take several days before one arrives in the field of ultra-high vacuum. But once the pumping and bake-out have been finished, the following instruments are at the disposal of the user:

- AFM/STM: due to the UHV environment, the resolution of these methods is greatly improved.
- Knudsen cell: the quality of the grown films benefits form the low vacuum as well. In growth heating can also be applied.
- LEED: besides AFM and STM techniques, *Low Energy Electron Diffraction* offers another way to acquire the crystalline configuration of the substrates and films.
- Button-heater: useful to clean samples or to conduct before/after growth annealing.

The JEOL has encountered many setbacks and obstacles over the course of this bachelor project. An addition of a short section in the result chapter to portray the capabilities of the UHV AFM shall be made. In the next chapter, the results obtained with the TRE and JPK AFM will be portrayed in an orderly fashion.

Chapter 5

Experimental Results

In this chapter, the results from different substrates shall be distinguished by dedicating an individual section to the $NaCl(001)$ and $BaF_2(111)$ substrates. In these sections, prior growth and after growth measurements shall be portrayed. The influencing factors shall be named appropriately and interesting features will be highlighted. At the end of this chapter, some results acquired with the JEOL will be presented.

The shown images are in general all height (trace or retrace) images. If otherwise, this will be explicitly mentioned. Moreover, the images were processed with the software *gwyddion*.

Furthermore, it is worth mentioning that the AFM measurements were conducted using cantilevers with a resonance frequency around the 300 kHz and an approximate force constant of 40 N/m. All Bismuth films were grown in the thermal evaporator using an average growth rate of 1 $\text{Å}/s$.

5.1 $NaCl$: substrate and grown film

First of all, the results concerning the $NaCl(001)$ shall be portrayed and investigated. Prior to the polishing, the surface of the sodium-chloride samples were measured under the JPK AFM. It was clear from these images the unpolished samples were unfit for growth due to big trenches and a relatively high surface roughness.

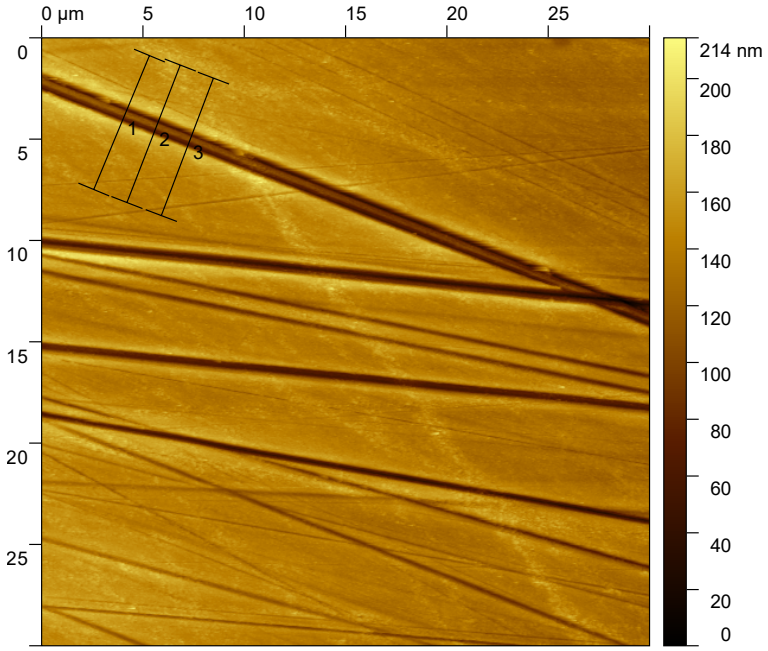

Figure 5.1: *AFM image (retrace) of the unpolished $NaCl$ with dimensions $30 \times 30\ \mu m$. These images were scanned with a scan rate of $1Hz$. The false color scale on the right gives an indication of the height differences.*

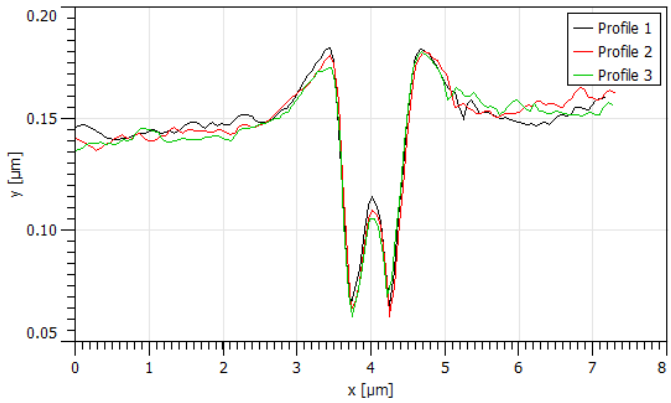

Figure 5.2: *Profile of the trench as indicated on the image above. The trench shows an approximate depth of 80 nm and a width of approximately 1 μm.*

On the same image, smaller trenches could also be found as seen in figure 5.3 and 5.4.

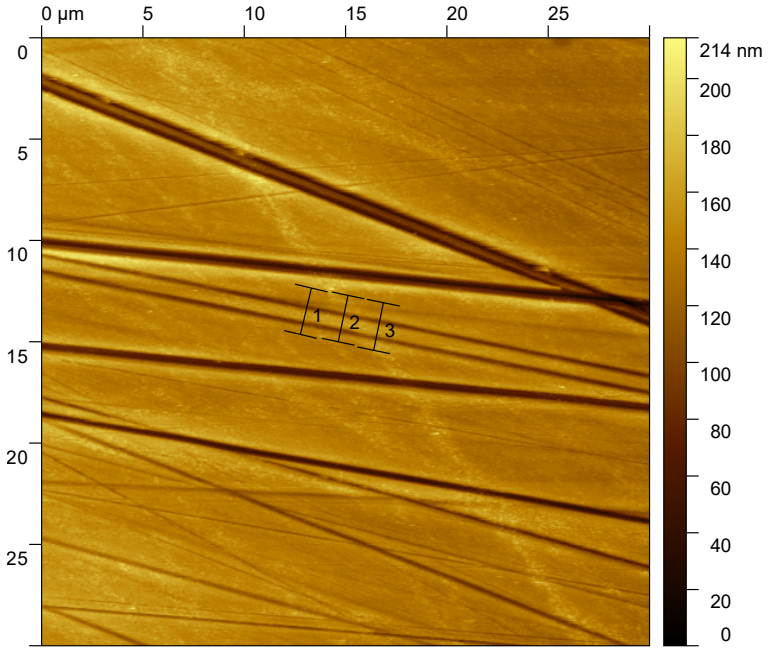

Figure 5.3: *AFM image (retrace) of the unpolished NaCl with dimension* 30×30 μm*. In this case, the smaller trenches are analyzed.*

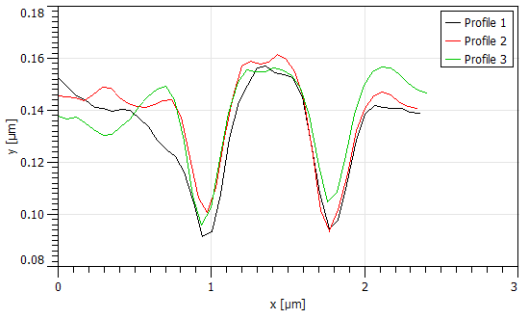

Figure 5.4: *Profile of the two trenches as indicated on the image above. These trenches shows an approximate depth of 60 nm and a width of approximately* $300 - 400$ nm*.*

The surface roughness along the diagonal (upper right to bottom left corner) of the image was $10,1$ nm and the trenches itself worsened the flatness. Thus, before growth could be accomplished, it was evident that these surfaces needed to be polished. This was done as described in section 4.1. The results of the polishing can be seen on the next page.

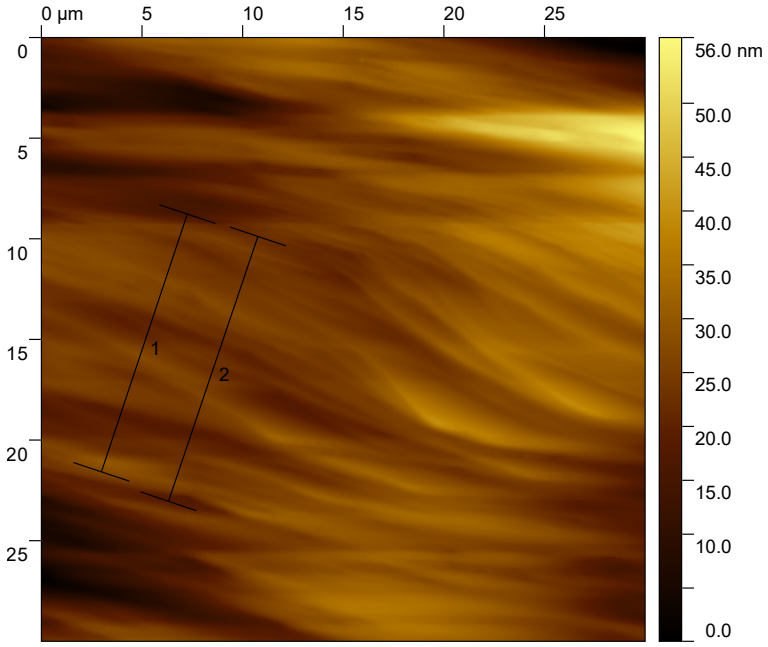

Figure 5.5: *AFM image (retrace) of the polished NaCl with dimension* 30×30 μm*. The deep trenches were removed and the emergence of what appear to be steps is visible.*

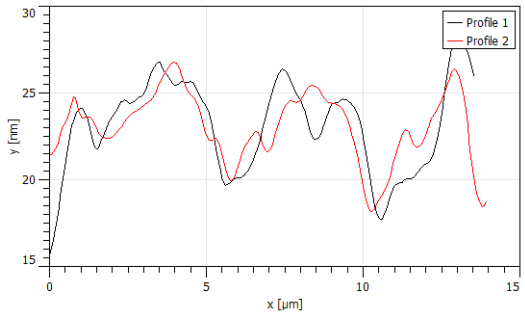

Figure 5.6: *Profile along the two lines as indicated on the image above. The roughness was greatly decreased by exterminating the trenches.*

Due to the polishing in the spin-coater with water and iso-propanol, the trenches were removed. The surface roughness along the diagonal improved to a value of 0,93 nm. The sodium-chloride samples could now be used as substrates for the growth of Bismuth thin films. However, the polishing could have been done in such a way that the plateaus were larger as can be seen in the paper of Payer et al [4].

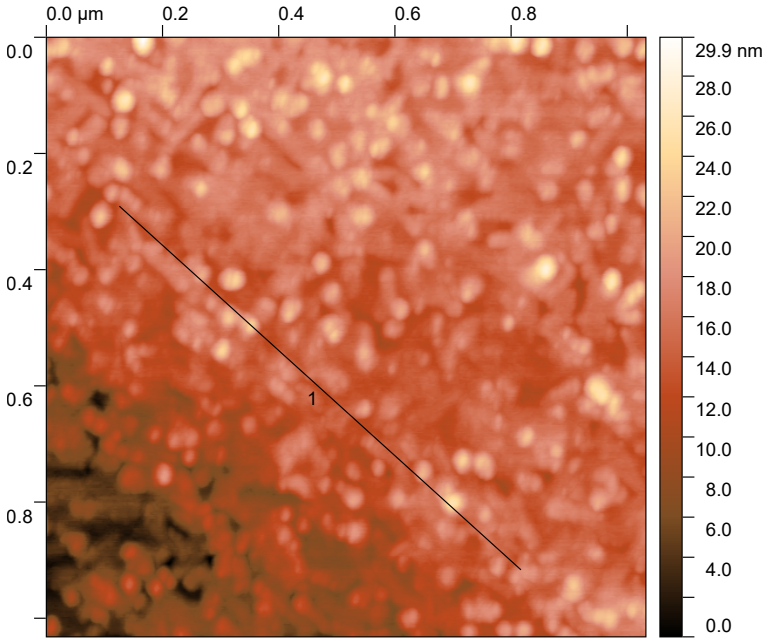

Figure 5.7: *AFM image (retrace) of the* $5\ nm$ *thick thin film of* Bi *with dimensions* $1,032 \times 1,032$ μm*. This film was grown on a polished* $NaCl$ *substrate and the formation of grains is clearly visible.*

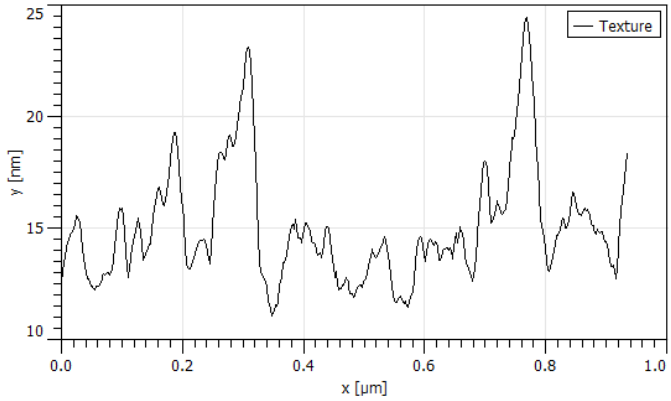

Figure 5.8: *Profile along the line as indicated on the image above. The grains show varying heights and sizes. The heights could reach values higher than the film thickness of* $5\ nm$*.*

As can bee seen from figure 5.8 the grains could reach heights that cross the inserted thickness of the film. This feature is theorized to be caused by the formation of grains and the way in which they grow [24]. The average surface roughness along the diagonal however was $0,88\ nm$.

5.2 BaF_2: substrate and grown film

Secondly, the results from the $BaF_2(111)$ samples shall be portrayed and investigated. Before the samples were cleaved, their surfaces were measured under the JPK AFM. The substrates, prior to cleaving, were unfit for growth due to dirt and the high surface roughness. This is evident from the next AFM image.

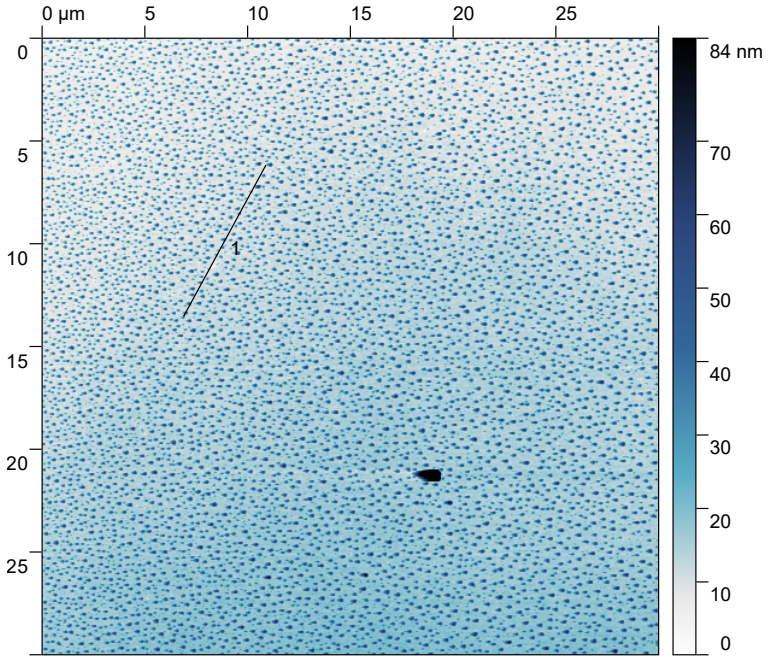

Figure 5.9: *AFM image (retrace) of the uncleaved BaF_2 substrate with dimensions 30×30 μm. The scan rate was $0,669$ Hz.*

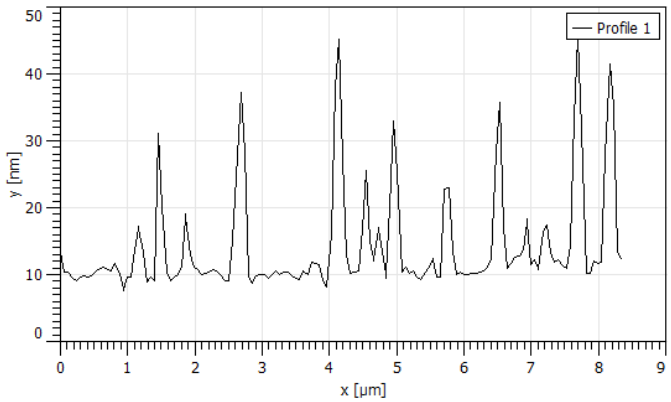

Figure 5.10: *Profile along the line as indicated on the image above. The dirt particles have relatively large heights and sizes and thus needed to be removed.*

This sample showed a surface roughness of $5,49\ nm$ along the diagonal. In between the dirt particles, usable patches were visible, but this wasn't an ultimate condition for growth. Therefore, the barium-fluoride samples were cleaved along the (111)-plane in order to improve the cleanliness and surface roughness of the samples. The result of the cleaving is presented on the next image.

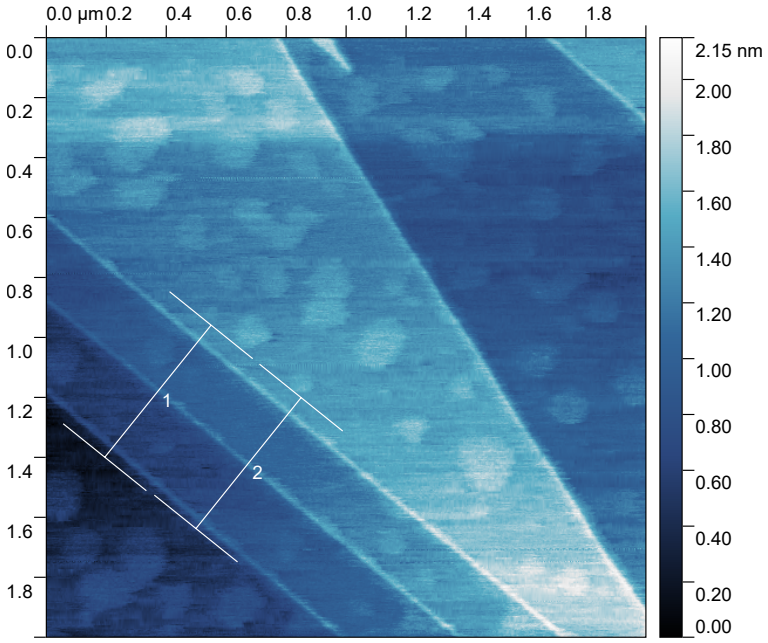

Figure 5.11: *AFM image (retrace) of the cleaved BaF_2 with dimensions $2 \times 2\ \mu m$. The scan rate was around the $1\ Hz$.*

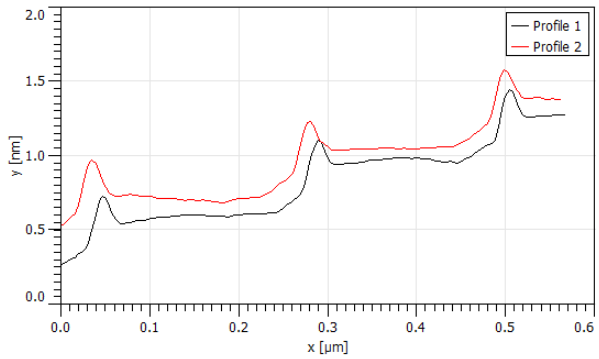

Figure 5.12: *Profile along the two lines as indicated on the image above. The steps are clearly visible and show a step size of approximately $0,365\ nm$.*

The cleaved sample turned out to be extremely flat with a surface roughness along the diagonal of $0,043\ nm$. The roundish features in the image are theorized to be water and other organic molecules. This wetting effect was previously seen by M. Cardellach, A. Verdaguer and J. Fraxedas [29].

The step-edges shall be revisited in the next AFM image.

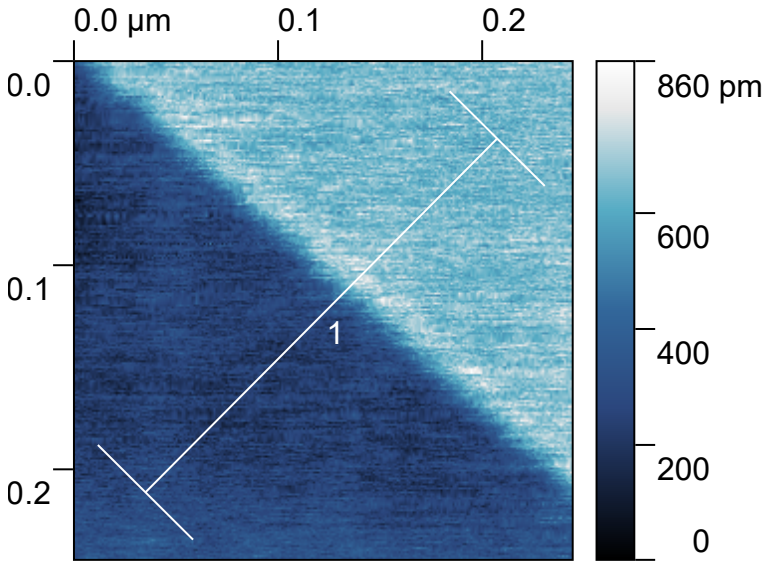

Figure 5.13: *AFM image (retrace) of cleaved $BaF2$ with dimensions of approximately* 250×250 *nm. The scan rate was around the* 1 *Hz.*

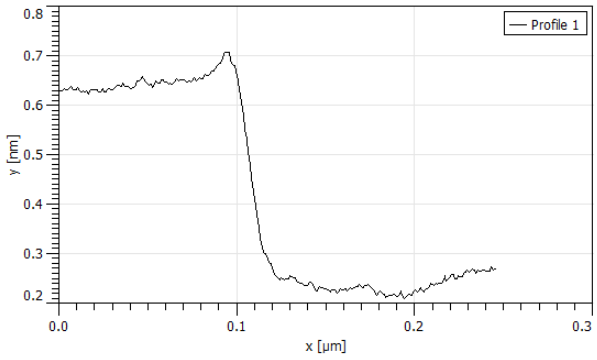

Figure 5.14: *Profile along the line as indicated on the image above. The two plateaus are visible and give a slightly larger step size of approximately* $0,42$ *nm.*

The reason for this step size difference might be measurement errors. However, these samples were extremely flat and very suitable for growth. The flat areas extend for several hundred of nano-meters and this is exactly what one would desire. On the next and last JPK AFM image, the growth of the film on these cleaved substrates will be investigated.

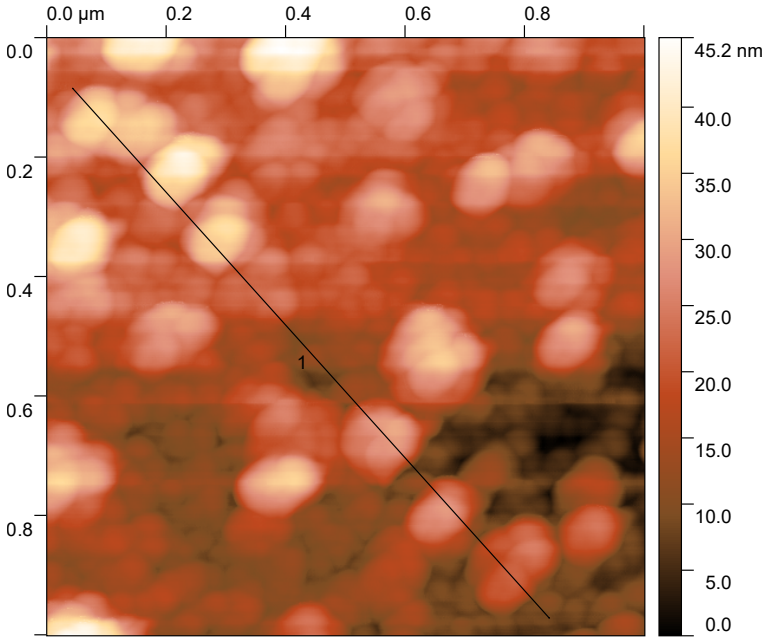

Figure 5.15: *AFM image (retrace) of the thin film of* $10\ nm$ *thick Bi grown on the cleaved barium-fluoride with dimensions of approximately* $1 \times 1\ \mu m$*. The scan rate was around the* 1 *Hz.*

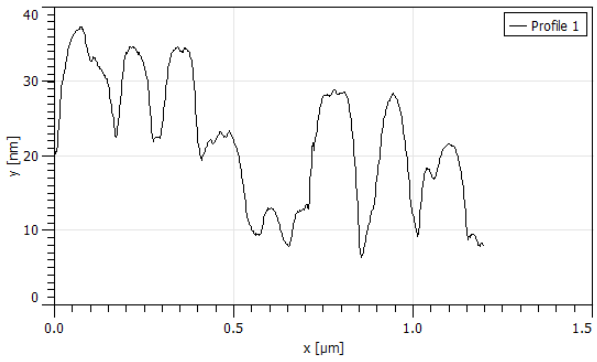

Figure 5.16: *Profile along the line as indicated on the image above. The grains could reach heights of* $10 - 20\ nm$ *and two-dimensional sizes of* $100 - 200\ nm$*. .*

The two-dimensional sizes of the grains formed on the cleaved barium-fluoride were notably larger than the ones formed on the polished sodium-chloride. The average surface roughness along the diagonal was $0,30\ nm$. The sizes of the grains are promising and they might have the same crystalline configuration. It is worth mentioning that this sample underwent two processes of thermal evaporation, in which twice a film of $5\ nm$ was deposited. After the first growth, the film wasn't visible and the conclusion was that no deposition had occurred. This conclusion is highly likable to be false, because a thin film of $5\ nm$ thick is barely visible. Therefore, the total grown film is expected to be around the $10\ nm$.

5.3 JEOL: improved Q-factor and AFM images

As promised at the beginning of this chapter, some results acquired with the JEOL shall be presented and discussed in this last section. Because the JEOL is a UHV system, one would expect higher Q-factors and therefore a higher resolution. The JEOL however still struggles with challenges that need to be resolved before it can truly show its potential.

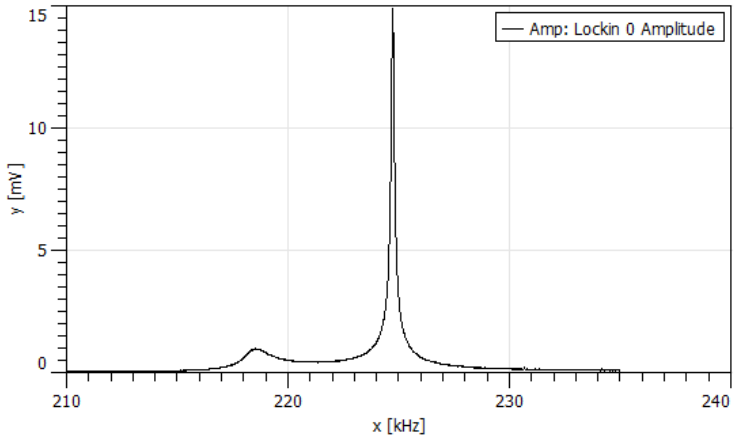

Figure 5.17: *Frequency sweep of a cantilever in the JEOL. The y-axes is in mV and the x-axes in kHz.*

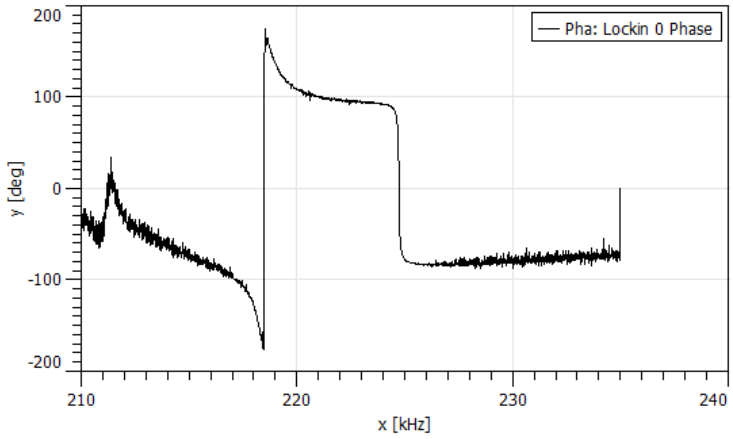

Figure 5.18: *Corresponding phaseshift of the frequency sweep as seen above. The y-axes is in degrees and the x-axes in kHz.*

The JEOL showed Q-factors ranging between $1000 - 3000$. However, the system still needs to be calibrated by measuring a characterized sample. Other tasks at hand are reducing the electrical noise by grounding the components properly and by further increasing the resolution in several ways. The inset on the next page will illustrate the kind of pictures we acquired while using the AFM of the JEOL.

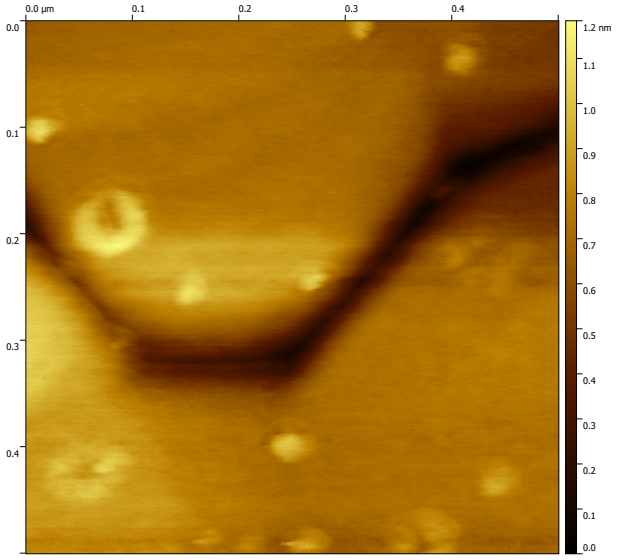

Figure 5.19: *AFM image (Height) of gold on mica with dimensions of approximately* 500×500 *nm.*

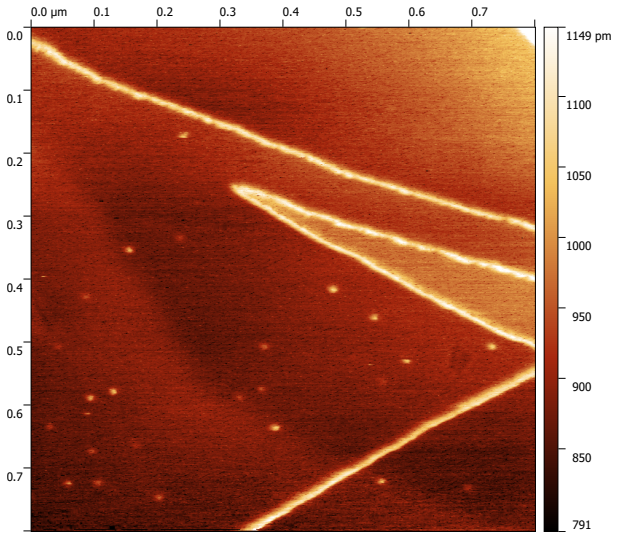

Figure 5.20: *AFM image (Height) of exfoliated HOPG with dimensions of approximately* 800×800 *nm.*

The indicated heights shown on the false color scale bars still need to be callibrated by looking at a known sample. In the image of gold on mica (top) the effect of electrical noise can clearly be seen. On the image of HOPG, the steps can be observed. The step edges turned out to be extremely dirty due to the high reactivity of the edges after exfoliation.

Chapter 6

Conclusion and Discussion

In conclusion, a couple of remarks concerning the results are appropriate to make.

- For instance, the polishing of the $NaCl$ crystal could have been executed better. While spinning the substrate, the water and iso-propanol should have been applied. In this case, the water and iso-propanol have not been applied while the substrate was spinning, but while it was standing still. Flat plateaus with an higher area could have been produced and thus improving the surface roughness [4]. This would have a positive effect on the film quality.
- The cleaving of the BaF_2 was successful. This produced ultra-flat patches which were optimal for growth.
- The grains formed on the BaF_2 samples were notably larger than the ones formed on the $NaCl$ samples. If these grains are crystalline (111), once could argue that the growth of the Bi thin films favors the barium-fluoride substrate.
- No epitaxial growth on the substrates was achieved. This is likely caused by the mono-layers of water and other molecules formed on the substrates before growth. The wetting phenomena was possibly observed on the BaF_2 substrate. This problem could be resolved by heating the substrates, thus out-gassing the mono-layers, in the TRE before growth.
- A system is needed to obtain the crystalline configuration of these grains. This can be executed with the JEOL in the future.
- Because no epitaxial growth was achieved on these substrates, the hypothesis concerning the 90 degrees rotational symmetry of the substrate lattices and the effect on the grown films remains untested.

Acknowledgements

This bachelor project was executed in the group of Jan van Ruitenbeek and under his supervision. I would like to thank my PhD supervisor Kim Akius for his help, patience and explanations. I shall never forget the following words spoken by mister Akius: *Do as I say, not as I do.* Working in UHV conditions takes patience, scrutiny and perseverance, but to one who perseveres, good things will come. Furthermore, I am immensely thankful for the continuous support of my family and friends.

Bibliography

[1] *Graphic of a 3D Topological Insulator*, Paul Scherrer Institute/Mahir Dzambegovic, Accessed: 16-07-2017.

[2] M. Cahay and S. Bandyopadhyay, *Introduction to Spintronics*, chapter 1, pages 1–13, CRC Press, 2008.

[3] T. Nagao, J. Sadowski, M. Saito, S. Yaginuma, Y. Fujikawa, T. Kogure, T. Ohno, Y. Hasegawa, S. Hasegawa, and T. Sakurai, *Nanofilm allotrope and phase transformation of ultrathin Bi film on Si(111)- 7x7*, Phys. Rev. Lett. **93** (2004).

[4] T. Payer, T. Rajković, M. Ligges, D. von der Linde, M. Horn-von Hoegen, and F.-J. Meyer zu Heringdorf, *Ultrathin epitaxially grown bismuth (111) membranes*, Appl. Phys. Lett. **93** (2008).

[5] S. Xiao, D. Wei, and X. Jin, *Bi(111) Thin Film with Insulating Interior but Metallic Surfaces*, Phys. Rev. Lett. **109** (2012).

[6] B. A. Bernevig, L. H. Taylor, and S.-C. Zhang, *Quantum Spin Hall Effect and Topological Phase Transition in HgTe Quantum Wells*, Science **314**, 1757 (2006).

[7] M. König, S. Wiedmann, C. Brüne, A. Roth, H. Buhmann, L. W. Molenkamp, X.-L. Qi, and S.-C. Zhang, *Quantum Spin Hall Insulator State in HgTe Quantum Wells*, Science **318**, 766 (2007).

[8] *Picture Sodium-Chloride*, `https://cs.wikipedia.org/wiki/Oxid_vanadnat%C3%BD`, Accessed: 13-07-2017.

[9] *Picture Barium-Fluoride*, `https://en.wikipedia.org/wiki/Barium_fluoride`, Accessed: 13-07-2017.

[10] N. Bourbaki, *Elements of Mathematics: General Topology*, Springer, 1995.

[11] C. Kane et al., *Topological Insulators*, chapter 1, pages 3–33, Elsevier, 2013.

[12] M. Z. Hasan and C. L. Kane, *Colloquium: Topological insulators*, Rev. Mod. Phys. **82**, 3045 (2010).

[13] Y. Ando, *Topological Insulator Materials*, J. Phys. Soc. Jpn. **82**, 1 (2013).

[14] F. Bloch, *Uber die Quantenmechanik der Elektronen in Kristallgittern*, Zeitschrift fur Physik **52**, 555 (1929).

[15] S.-S. Chern, *Characteristic Classes of Hermitian Manifolds*, Annals of Mathematics **47**, 85 (1946).

[16] C. Kane and E. J. Mele, Z_2 *Topological Order and the Quantum Spin Hall Effect*, Phys. Rev. Lett. **95** (2005).

[17] A. Akhmerov, J. Sau, B. van Heck, B. Nijholt, I. Muhammad, and T. O. Rosdahl, *Course: DelftX: TOPOCMx Topology in Condensed Matter: Tying Quantum Knots*, https://www.edx.org/course/topology-condensed-matter-tying-quantum-delftx-topocmx-0 (Link to license: https://creativecommons.org/licenses/by-sa/4.0/legalcode. No crucial adjustments have been made, the work has been rephrased in an appropriate manner.).

[18] *Image representing genus*, `https://www.learner.org/courses/mathilluminated/units/4/textbook/03.php`, Accessed: 13-07-2017.

[19] A. Cayley, *On the theory of permutants*, Cambridge and Dublin Mathematical Journal **7**, 40 (1852).

[20] L. Fu and C. L. Kane, *Time reversal polarization and a* Z_2 *adiabatic spin pump*, Phys. Rev. B **74** (2006).

[21] A. Manchon, H. C. Koo, J. Nitta, S. M. Frolov, and R. A. Duine, *New perspectives for Rashba spin-orbit coupling*, Nature **14**, 871 (2015).

[22] P. Hofmann, *The surfaces of bismuth: Structural and electronic properties*, Progress in Surface Science **81**, 191 (2006).

[23] S. Murakami, *Quantum Spin Hall Effect and Enhanced Magnetic Response by Spin-Orbit Coupling*, Phys. Rev. Lett. **97** (2006).

[24] M. Ohring, *Materials Science of Thin Films*, chapter 7, pages 357–360, Academic Press, 2001.

[25] G. Haugstad, *Atomic Force Microscopy: Understanding Basic Modes and Advanced Applications*, chapter 1, pages 1–32, John Wiley & Sons, Inc, 2012.

[26] *Laser alignment, picture is not the fabrication of the author*, `http://experimentationlab.berkeley.edu/AFM`, Accessed: 14-07-2017.

[27] *Schematic of a Thermal Resistive Evaporator, manually changed to better represent the LION set-up.*, `http://pubs.rsc.org/en/content/chapterhtml/2014/bk9781849736381-00001?isbn=978-1-84973-638-1`, Accessed: 14-07-2017.

[28] M. Ohring, *Materials Science of Thin Films*, chapter 3, pages 95–140, Academic Press, 2001.

[29] M. Cardellach, A. Verdaguer, and J. Fraxedas, *Defect-induced wetting on* $BaF_2(111)$ *and* $CaF_2(111)$ *at ambient conditions*, Surface Science **605**, 1929 (2011).